Journal of Materials Science & Technology 123 (2022) 92–112

Contents lists available at ScienceDirect

Journal of Materials Science & Technology

journal homepage: www.elsevier.com/locate/jmst

Research Article

Effect of post weld artificial aging and water cooling on microstructure and mechanical properties of friction stir welded 2198-T8 Al-Li joints

Y. Tao, Z. Zhang, P. Xue, D.R. Ni*, B.L. Xiao, Z.Y. Ma*

Institute of Metal Research, Chinese Academy of Sciences, Shenyang 110016, China

ARTICLE INFO

Article history:
Received 1 November 2021
Revised 14 December 2021
Accepted 19 January 2022
Available online 24 March 2022

Keywords:
Friction stir welding
Aluminum-lithium alloys
Microstructure
Mechanical properties

ABSTRACT

Friction stir welding (FSW) under both air cooling and water cooling conditions with welding parameters of 800–1200 rpm rotation rates and 50–200 mm/min welding speeds was carried out on 2198-T8 Al-Li alloys, and post weld artificial aging was performed on the air cooled joints. No welding defects other than lazy S were observed in the nugget zone (NZ) for all joints. Under air cooling condition, the lowest hardness zone (LHZ) occurred in the heat affected zone (HAZ). FSW resulted in gradual dissolution of original T_1, θ' and δ'/β' from the base material (BM) to the thermo-mechanically affected zone (TMAZ), and complete dissolution of all precipitates in the NZ with δ'/β' and Guinier-Preston zones precipitating during cooling. The air cooled joints exhibited no noticeable changes in intrinsic tensile strength with a joint strength reaching 81.3% of the BM, but varied elongation with welding parameters, which was closely related to failure in the NZ and fracture along lazy S. Post weld artificial aging led to the largest hardness recovery in the TMAZ but smaller hardness recovery in the initial LHZ and the NZ. Different aging kinetics across the joint was determined by volume fraction of both original precipitate dissolution during welding and coarse particles formed during aging, and by dislocation density inherited from welding. Post weld artificial aging greatly enhanced the joint strength with the ultimate tensile strength reaching 87.3% of the BM. As compared to air cooling condition, water cooling hardly affected the NZ hardness and did not improve the joint strength, and the reason was discussed in light of precipitates, hardness changes and fracture behavior.

1. Introduction

The growing need for materials with high strength and low density for aerospace applications has led to a great interest in aluminum-lithium (Al-Li) alloys, as the density of Al alloys was decreased by 3% and the elastic modulus was enhanced by about 6% with each 1 wt.% Li addition [1]. Since the first generation of Al-Li alloys was developed in the 1950s, these materials have experienced three generations [1]. However, due to disadvantages such as anisotropy in mechanical properties, low toughness and poor corrosion resistance, the previous two generations did not find wide use in aerospace industry [1,2]. To overcome these shortcomings, the latest (third) generation Al-Li alloys have been developed over the last decade, which have higher Cu/Li ratio and are alloyed with other elements such as Mg, Ag, Mn and Zn [1,3].

The introduction of welding into aircraft components offers further weight and cost benefits by replacing riveting and mechanically fastened joints [4–6]. As an innovative solid-state joining technique invented in 1991, friction stir welding (FSW) intrinsically eliminates solidification cracks and porosities encountered in fusion welding of Al alloys and can produce joints with lower distortion and higher strength than fusion welding because of lower heat input [7,8]. FSW is the most appealing welding process in aeronautical structures when applied to Al alloys and has proved to succeed in producing reliable Al-Li alloy joints [4,9–11].

Although FSW generates considerably lower heat input in the joints than fusion welding, strength loss of the joints for precipitation-hardened Al alloys seems inevitable even under optimized welding parameters [12–14]. Previous studies indicated that post weld heat treatment and water cooling were effective ways for improving mechanical properties of FSW joints for conventional precipitation-hardened Al alloys [12,15–21]. As compared to conventional precipitation-hardened Al alloys, Al-Li alloys exhibit a wider variety of precipitates (δ' (Al_3Li), T_1 (Al_2CuLi), θ' (Al_2Cu), S' (Al_2CuMg), etc.), depending upon alloy composition and heat treatment conditions [14,17,22,23]. As a result, changes in heat input may give rise to complex variations in precipitation behavior and hence mechanical properties for FSW Al-Li joints. However, very

* Corresponding authors.
E-mail addresses: drni@imr.ac.cn (D.R. Ni), zyma@imr.ac.cn (Z.Y. Ma).

https://doi.org/10.1016/j.jmst.2022.01.020
1005-0302/

little information about the effect of post weld heat treatment and water cooling on FSW Al-Li joints has been reported so far [24–28].

Sidhar et al. [26] reported that for FSW joints of peak aged 1424 Al-Li alloy, both post weld artificial aging and water cooling led to considerable improvement in tensile strength accompanied by reduction in ductility. Besides, post weld artificial aging resulted in full recovery of hardness across the joint, whereas water cooling reduced the extent of hardness loss in the heat affected zone (HAZ) but had very small effect on the hardness of the nugget zone (NZ). However, in another study on FSW joints of 2195-T8 and 2199-T8 Al-Li alloys, Sidhar and Mishra [27] indicated that post weld artificial aging brought about different levels of hardness recovery in the HAZ, thermo-mechanically affected zone (TMAZ) and NZ. Unfortunately, tensile properties of the joints were not addressed in this article. Zhang et al. [28] studied the effect of post weld solution treatment followed by artificial aging on FSW 2195-T8 Al-Li joints. They pointed out that although the hardness and the tensile strength of the joint were significantly improved after heat treatment, the NZ and the TMAZ exhibited abnormal grain growth, which caused dramatic deterioration in ductility.

It is evident from literature, post weld heat treatment could result in distinctly different hardness changes for FSW joints of different Al-Li alloys, which might be linked to the nature of predominant precipitates and alloying elements. Moreover, only scarce research work has been devoted so far to the microstructure-mechanical property correlations of FSW Al-Li joints during post weld heat treatment or water cooling [26].

Alloy 2198, one of the third generation Al-Li alloys, is developed to replace 2024Al and 2524Al alloy in aircraft structures and shows a good combination of static tensile properties, damage tolerance and formability [1]. In recent years, there has been some effort to study the microstructure and mechanical properties of FSW 2198-T8 joints [29–34] and the main findings are concluded as follows.

Firstly, the precipitate evolution of FSW 2198-T8 joints was complicated and conflicting results were reported in different studies. Gao et al. [29] reported that the base material (BM) was composed of T_1, S′, θ' and δ', and the NZ contained only δ'. However, Nayan et al. [32] found that the BM consisted merely of T_1, while the NZ showed T_1, β' (Al_3Zr) and Guinier-Preston (GP) zones. In addition, Rao et al. [33] pointed out that the NZ was characterized by T_1, T_B (Al_7Cu_4Li) and δ'. Secondly, opinions were divided on the tensile strength variations with welding parameters for FSW 2198-T8 joints. Rao et al. [33] and Nayan et al. [32] reported that the joint strength was hardly affected by rotation rate, whereas Li et al. [31] found that the joint strength first increased and then decreased with increase in rotation rate to welding speed ratio. Moreover, detailed explanations about the influencing mechanism of welding parameters on the joint strength are lacking. Thirdly, the tensile fracture of FSW 2198-T8 joints could occur in the TMAZ [30] or the NZ [31,34] and the latter did not correspond to the lowest hardness zone (LHZ).

The above studies indicated that the precipitate evolution, the tensile strength changes with welding parameters and the fracture behavior of FSW 2198-T8 joints remained controversial. Thus, a thorough investigation aimed at elucidating the welding parameter-microstructure-mechanical property relationships for FSW 2198-T8 joints is still highly desired. Furthermore, the influence of post weld heat treatment and water cooling on FSW 2198-T8 joints has not been studied yet.

In this study, 2198-T8 alloy was subjected to FSW under rotation rates of 800–1200 rpm and welding speeds of 50–200 mm/min, and the relationship between microstructure and mechanical properties was investigated in detail. The objective of the present work is to clarify the following issues using FSW 2198-T8 joints: (a) the microstructure evolution and the influencing mechanism of welding parameters on the mechanical properties for the as-welded joints; (b) the effect of post weld heat treatment and water cooling on the microstructure of the joints and its correlation with the mechanical properties.

2. Experimental procedures

The BM used in the present study was a rolled 2198-T8 alloy, 3.2 mm in thickness. Its composition was Al-0.94Li-3.37Cu-0.31Mg-0.27Ag-0.15Zr (wt.%). Before welding, both top and butt surfaces of the plates were cleared by abrasive papers. The plates were friction stir welded along the rolling direction. Three welding parameters, i.e., 800 rpm-200 mm/min, 1200 rpm-200 mm/min and 1200 rpm-50 mm/min were employed. The welding tool consisted of a 12.0 mm-diameter concave shoulder and a 4.0 mm-root diameter and 3.0 mm-length pin with threaded cone shape. A shoulder plunge depth of about 0.2 mm was controlled during FSW. The schematic drawing of FSW and shape of the welding tool are shown in Fig. 1. The plates for welding and the sink were fixed in the operation floor during FSW with clamps, which consisted of nuts, bolts, fixture blocks and rubber gaskets.

FSW experiments were performed under two cooling conditions: (a) normal air cooling and (b) submerged water cooling by immersing welding tools and plates into room temperature (i.e., 20 °C) flowing water during FSW. Additionally, artificial aging was applied to the joints under air cooling condition immediately after welding. Post weld artificial aging was conducted by heating the joints in an air furnace at 180 °C for 24 h. Abbreviated forms were adopted to designate FSW samples, as shown in Table 1. For example, the sample welded under 800 rpm–200 mm/min in air cooling condition, followed by artificial aging at 180 °C for 24 h, were denominated as sample AC-800-200-AA. Examinations of microstructure and mechanical properties were performed after natural aging at room temperature for at least two months.

Vickers hardness tests were conducted by using an automatic testing machine (LECO, LM-247AT) with a 500 g load for 10 s. Cross sectional samples for hardness tests were cut perpendicular to the welding direction followed by grinding and polishing. Hardness profiles of the joints were performed along mid-thickness of the cross section with an interval of 1 mm. Tensile samples with a gauge length of 35 mm were machined perpendicular to the welding direction, the configuration of which is shown in Fig. 2 and has beenreported previously [34]. In order to acquire the intrinsic tensile properties and failure location of the joints, a smooth surface and an equal cross-sectional area across the gauge part for tensile samples were achieved by grinding the samples with abrasive papers. Zwick-Roell testing machine was used for tensile tests under a strain rate of 1×10^{-3} s^{-1}. Three tensile samples were tested for each welding condition. Scanning electron microscopy (SEM, Quanta 600) was used for observations of fracture surfaces.

Grain structures of the joints were observed by optical microscopy (OM, Axiovert 200 MAT). After being ground and polished, samples for OM were etched by Keller's reagent, which was composed of 2 ml hydrofluoric acid, 3 ml hydrochloric acid, 5 ml nitric acid and 190 ml water. Transmission electron microscopy (TEM, TECNAI 20) was employed to characterize precipitation behavior across the joints. Thin disks for TEM were ground and then twin-jet electropolished using a solution of 125 ml nitric acid and 375 ml methanol at −25 °C and 10 V. The location-to-location correspondence between hardness measurements and TEM observations was carefully ensured by following these steps. Firstly, the samples after hardness tests were etched to reveal the correlation between the indentation position and the hardness value for each hardness indentations. Secondly, representative locations from the BM to the NZ were chosen for TEM observations according to hardness indentations and marked with white dots. Thirdly, thin disks

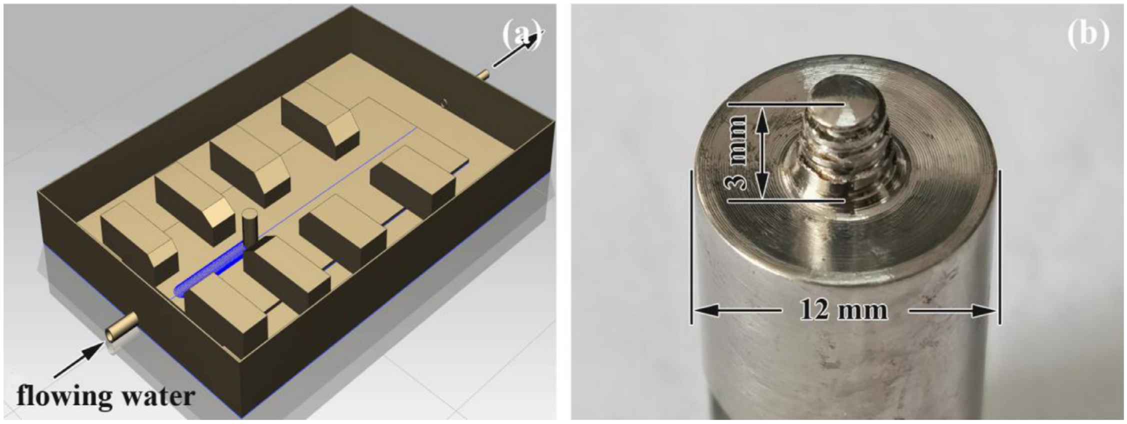

Fig. 1. (a) Schematic drawing of FSW and (b) shape of the welding tool.

Table 1
Welding parameters of FSW 2198-T8 joints.

Cooling method	Rotation rate(rpm)	Traverse speed(mm/min)	Designation
Air cooling	800	200	AC-800–200
	1200	200	AC-1200–200
	1200	50	AC-1200–50
Air cooling, followed by post weld artificial aging	800	200	AC-800–200-AA
	1200	200	AC-1200–200-AA
	1200	50	AC-1200–50-AA
Water cooling	800	200	WC-800–200
	1200	200	WC-1200–200
	1200	50	WC-1200–50

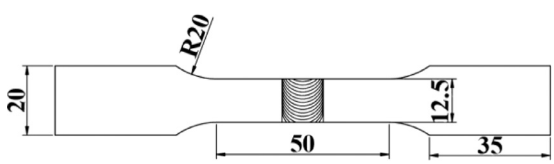

Fig. 2. Configuration and size of the tensile sample.

for TEM were cut from these locations with great care and make sure that the white marks were located in the middle of the disks.

3. Results

Cross-sectional macrographs of FSW 2198-T8 joints under air cooling and water cooling conditions are shown in Fig. 3. No welding defects except for a preferentially etched wavy line, often referred to as “lazy S” [35–37], are observed in the NZ for all the joints investigated. With increasing the rotation rate or decreasing the welding speed, lazy S becomes fainter and more discontinuous. It should be noted that lazy S remains in the upper part of the NZ under all the welding parameters investigated. Moreover, the lazy S close to the joint surface is strongly tilted with respect to the transverse direction and the tilting angle varies with welding parameters. Water cooling does not exert an obvious effect on the shape of lazy S but reduces the width of the NZ as compared to air cooling condition.

The origin and microstructure of lazy S have already been well reported by previous researchers [36–40]. In general, lazy S was revealed to originate from oxide layer on initial butt surfaces of the plates [38,40]. Moreover, detailed TEM characterization of lazy S by Sato et al. [40] showed that lazy S consisted of a high density of fine Al_2O_3 particles. It should be pointed out that lazy S could hardly be detected by OM and SEM before etching. In the present study, typical microstructures of lazy S after etching by OM and SEM are shown in Fig. 4. The presence of lazy S in the NZ is due to contrast difference between the matrix and the locally and densely distributed micro-cavities, which result from exfoliation of numerous fine oxide particles during etching [36,40]. These observations are consistent with the results obtained in FSW 1050-H24Al joints and FSW Al-Mg-Sc joints [36,40].

Optical microstructures of various zones of the joints are shown in Fig. 5. The BM consists of band-like grains relating to rolling processes. For sample AC-800-200, the grain morphology and size of the HAZ are similar to those of the BM. The grains in the TMAZ are deformed and upward-rotated due to the strain induced by stirring motion of the welding tool. The NZ exhibits fine and equiaxed recrystallized grains arising from severe plastic deformation and thermal exposure during welding. Post weld artificial aging hardly changes the microstructure of the HAZ, but leads to recrystallizaiton in the TMAZ and more equiaxed grains in the NZ for sample AC-800-200-AA. As compared to air cooling condition, water cooling does not bring about apparent changes in the microstructures of various zones for sample WC-800-200, except for the slight decrease in grain size of the NZ.

Fig. 6 depicts hardness profiles of the joints under different conditions. Fig. 6(a) shows the effect of welding parameters on the hardness profiles for the air cooled joints. In general, the hardness falls sharply within the HAZ before reaching a minimum at $\sim$ 6 mm from weld center (i.e., the LHZ), which is still located in the HAZ, and then rises through the TMAZ up to the NZ. With increasing the rotation rate or decreasing the welding speed, the LHZ hardness decreases, while the NZ hardness remains almost unchanged.

The effects of post weld artificial aging and water cooling on the hardness profiles of the joints at 800 rpm–200 mm/min, 1200 rpm–200 mm/min and 1200 rpm–50 mm/min are shown in Fig. 6(b-d), respectively. Overall, post weld artificial aging leads to considerable increase in hardness throughout the weld. However, it is worth noting that such an increase in hardness is the largest in the TMAZ and relatively smaller in the initial LHZ as well as the

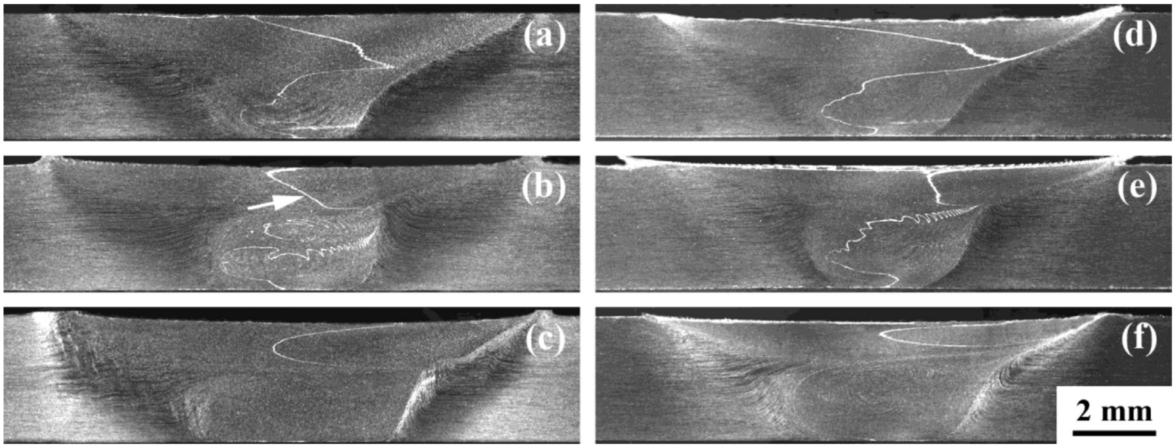

Fig. 3. Cross-sectional macrographs of FSW 2198-T8 joints: (a) AC-800–200, (b) AC-1200–200, (c) AC-1200–50, (d) WC-800–200, (e) WC-1200–200 and (f) WC-1200–50.

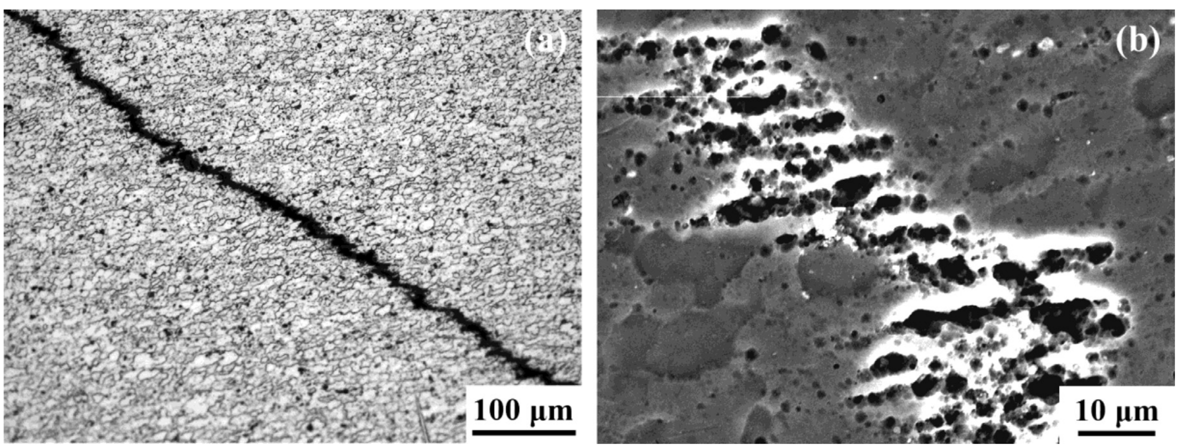

Fig. 4. Micrographs of lazy S in the areas marked by arrows in Fig. 3(b): (a) OM image and (b) magnified SEM image.

Table 2
Transverse tensile properties of FSW 2198-T8 joints.

Sample	UTS (MPa)	YS (MPa)	El. (%)	Joint efficiency (%)
BM	488.5 ± 0.2	417.5 ± 21.9	16.9 ± 0.5	–
AC-800–200	397.2 ± 0.1	262.3 ± 6.5	9.1 ± 0.2	81.3
AC-800–200-AA	423.9 ± 0.5	386.1 ± 0.4	4.5 ± 0.4	86.8
WC-800–200	384.9 ± 0.6	277.1 ± 0.6	8.0 ± 0.3	78.8
AC-1200–200	388.9 ± 4.8	271.2 ± 0.0	6.0 ± 0.4	79.6
AC-1200–200-AA	426.5 ± 2.0	387.4 ± 1.2	3.2 ± 0.7	87.3
WC-1200–200	390.6 ± 3.5	286.3 ± 1.9	5.0 ± 0.4	80.0
AC-1200–50	388.7 ± 1.9	256.6 ± 2.7	9.0 ± 0.3	79.6
AC-1200–50-AA	410.7 ± 1.2	358.5 ± 1.2	4.2 ± 0.4	84.1
WC-1200–50	379.7 ± 1.9	267.9 ± 0.6	7.4 ± 1.1	77.7

NZ. Hence the LHZ of the post weld aged joints occurs in either the initial LHZ or the NZ. Water cooling results in narrowed softened region and shifts the LHZ from the HAZ to the TMAZ as compared to air cooling condition. Nevertheless, the NZ hardness is hardly affected or decreases only marginally by water cooling.

Transverse tensile properties of FSW 2198-T8 joints in various conditions are shown in Table 2 and three important findings could be revealed. Firstly, for the air cooled joints, the ultimate tensile strength (UTS) does not exhibit conspicuous changes with variation in welding parameters with the UTS of sample AC-800-200 being slightly higher. However, the elongation of sample AC-1200-200 is lower as compared to that of samples AC-800-200 and AC-1200-50. The joint efficiency, defined as the ratio of UTS of the joint to that of the BM, could reach 81.3% under the investigated welding parameters, which is the highest reported so far for FSW 2198-T8 joints [30–32,41]. Secondly, post weld artificial aging greatly enhances the joint strength for all welding parameters with the joint efficiency being increased up to 87.3%. However, post weld artificial aging leads to ductility deterioration for all joints. Thirdly, water cooling does not exert an obvious effect on tensile properties of the joints as compared to air cooling condition.

Aiming at revealing the exact fracture locations of the joints, the cross-sections of the fractured samples were etched (Fig. 7). The main results could be summarized as follows. Firstly, in both air cooling and water cooling conditions, all joints fracture in the NZ rather than the LHZ (Fig. 7(a–c, g–i)), which corresponds to the HAZ for air cooling condition and the TMAZ for water cooling condition. Nevertheless, for FSW joints of conventional precipitation-hardened Al alloys, the fracture usually took place in the LHZ [42–48]. Secondly, in the case of post weld aging condition, the frac-

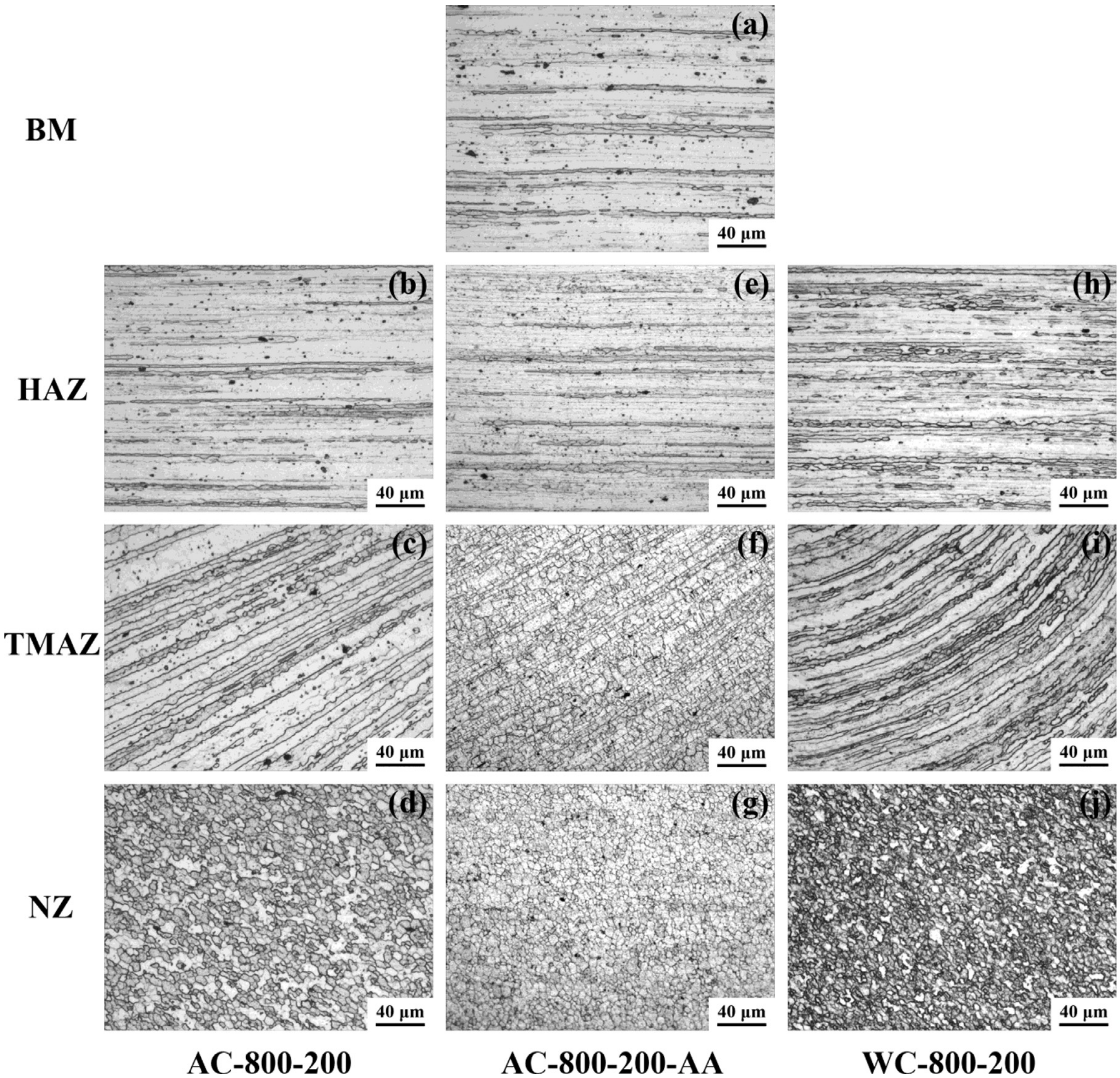

Fig. 5. Optical micrographs of various zones of FSW 2198-T8 joints.

ture either occurs in the NZ for samples AC-800-200-AA and AC-1200-200-AA (Fig. 7(d, e)) or stretches across the NZ to the HAZ for sample AC-1200-50-AA (Fig. 7(f)), which are all consistent with the LHZ. Thirdly, for air cooling, water cooling and post weld aging conditions, the fracture is partially along lazy S for joints at 1200 rpm–200 mm/min with their coincident part lying in the upper part of the NZ (indicated by arrows in Fig. 7), while it is independent of lazy S for joints at 800 rpm–200 mm/min and 1200 rpm–50 mm/min.

For all welding parameters, fracture surfaces of the joints under air cooling, post weld aging and water cooling conditions were carefully examined by SEM to reveal the difference in fractographs. Considering that joints at 800 rpm–200 mm/min and 1200 rpm–50 mm/min exhibit almost the same fracture feature, so only the results at 1200 rpm–200 mm/min and 1200 rpm–50 mm/min were presented on behalf of two kinds of fracture paths, i.e., partially along lazy S and independent of lazy S, respectively.

Macrographic fractographs of the joints at 1200 rpm–200 mm/min and 1200 rpm–50 mm/min under various conditions are shown in Fig. 8. Samples AC-1200-200, AC-1200-200-AA and WC-1200-200 show similar uneven fracture surfaces with a distinct pattern appearing in the upper part of the NZ (marked by arrows in Fig. 8(a, c, e)), which corresponds well to the area failed along lazy S, as marked by arrows in Fig. 7. However, the fracture surfaces are all flat for samples AC-1200-50, AC-1200-50-AA and WC-1200-50, but the middle portion of sample AC-1200-50-AA exhibits smoother appearance than other portions (Fig. 8(b, d, f)).

For samples AC-1200-200, AC-1200-200-AA and WC-1200-200, magnified images of the area failed along lazy S (marked by arrows in Fig. 8(a, c, e)) have roughly the same fracture feature and are characterized by lots of shallow submicron dimples (Fig. 9(a, b)), which is consistent with SEM observations reported in previous studies [36]. Nevertheless, magnified images of other areas with the fracture path away from lazy S show larger and deeper dimples at both position A for sample AC-1200-200 and position C for sample WC-1200-200 (Fig. 9(c, e)), but typical intergranular fracture feature at position B for sample AC-1200-200-AA (Fig. 9(d)).

The fracture features of positions D, E and G for samples AC-1200-50, AC-1200-50-AA and WC-1200-50 (Fig. 10(a, b, d)) are similar to those of positions A, B and C, i.e., the areas failed away from lazy S, for sample AC-1200-200, AC-1200-200-AA and WC-1200-200 (Fig. 9(c–e)), respectively. It should be pointed out that the fracture feature is strongly related to the grain morphology. Since positions E and F for sample AC-1200-50-AA are located in

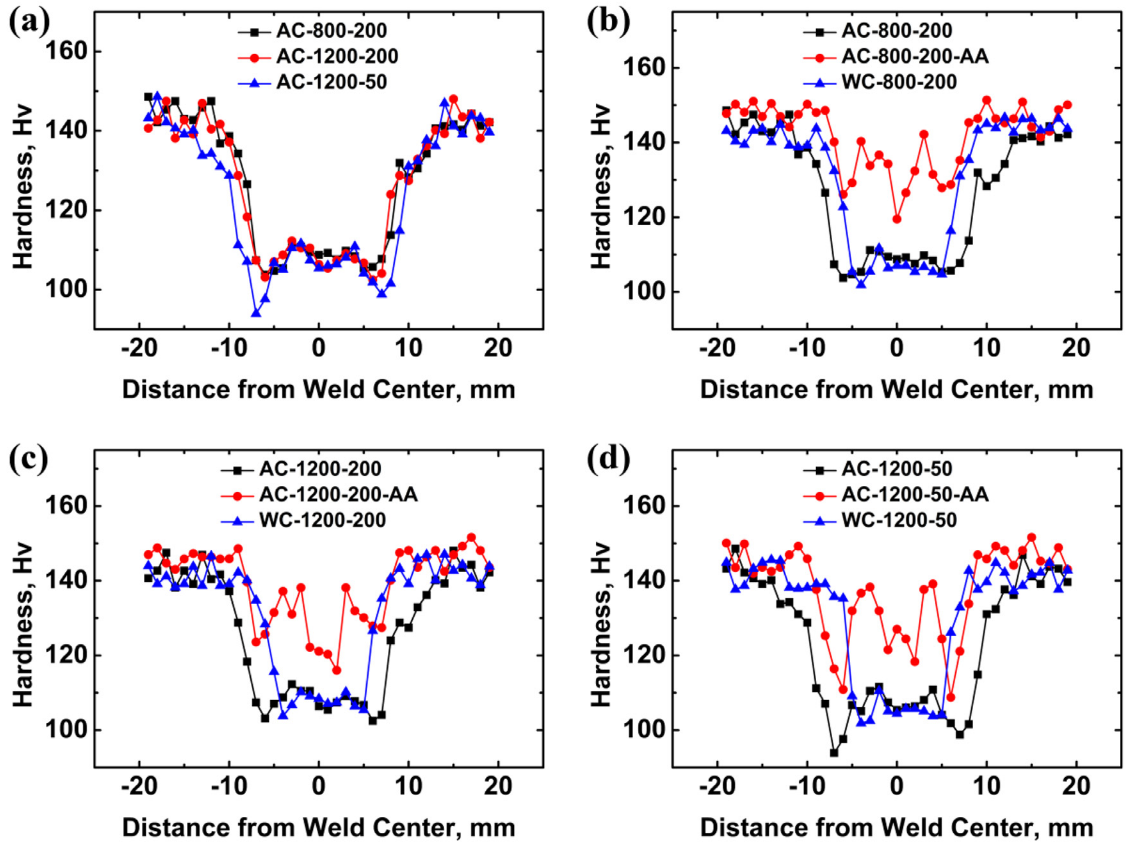

Fig. 6. Hardness profiles of FSW 2198-T8 joints exhibiting (a) effect of welding parameter under air cooling condition; effect of post weld artificial aging and water cooling at (b) 800 rpm–200 mm/min, (c) 1200 rpm–200 mm/min and (d) 1200 rpm–50 mm/min.

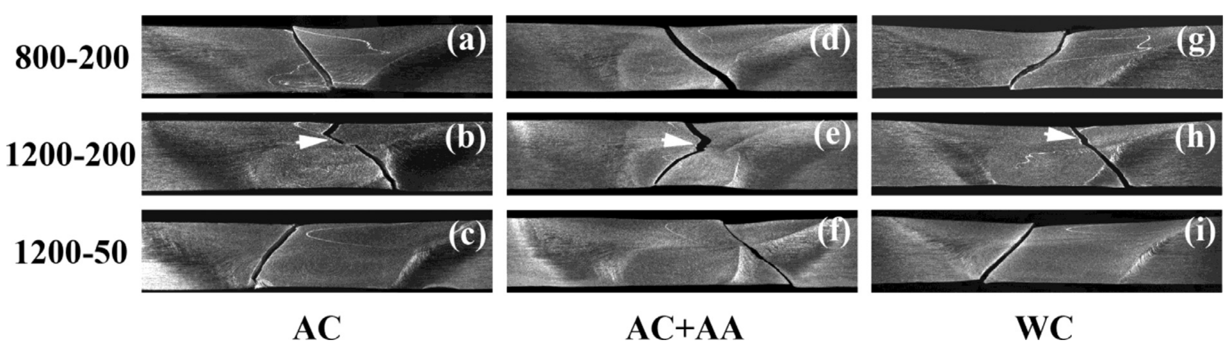

Fig. 7. Fracture locations of FSW 2198-T8 joints at various parameters.

the NZ with fine equiaxed grains and the TMAZ with upward-rotated band-like grains, respectively (Figs. 7(f) and 6(d)), they display absolutely different fracture features although they both belong to intergranular fracture (Fig. 10(b, c)).

To reveal the reason for hardness variations from the BM to the NZ for the air cooled joint and for different levels of hardness recovery throughout the weld after post weld artificial aging, detailed precipitate characterization was conducted on representative locations by TEM under both air cooling and post weld aging conditions. These locations corresponded to (a) the BM, (b) 6 mm from the weld center in the HAZ, i.e., the LHZ, (c) 4 mm from the weld center in the TMAZ, corresponding to the hardness peak within the softened region of the post weld aged joints and (d) the weld center in the NZ. In addition, since both the air cooled and the water cooled joints fracture in the NZ during tensile tests (Fig. 7), the NZ is of particular interest and thus TEM observations of the NZ in the case of water cooling condition were also performed. Joints at 800 rpm–200 mm/min were used for TEM examination under the above three conditions.

The typical precipitates expected in Al-Cu-Li-Mg-Ag-Zr alloys are T_1, θ', S', δ', β' (Al_3Zr) and GP zones [22,49]. Table 3 shows the precipitation characteristics of these precipitates. The precipitate identification was achieved with the help of the selected area diffraction (SAD) patterns according to three Al zone axes: <100>, <110> and <112>. The schematic diagrams of SAD patterns for the precipitates mentioned above have been reported previously by the present authors in a study on FSW 2060-T8 Al-Li joints [50].

TEM bright field micrographs and SAD patterns reveal the presence of T_1, θ' and δ' or β' precipitates in the BM (Fig. 11). T_1 is the dominant strengthening precipitates in the BM, present as hexagonal platelets on $\{111\}_{Al}$ habit planes [51]. When viewing along $<110>_{Al}$ zone axis, two variants of T_1 occur as needles lying along $<111>_{Al}$ direction (Fig. 11(b)) [4,9]. T_1 could be identified readily by its characteristic reflections and streaks, e.g., the four sym-

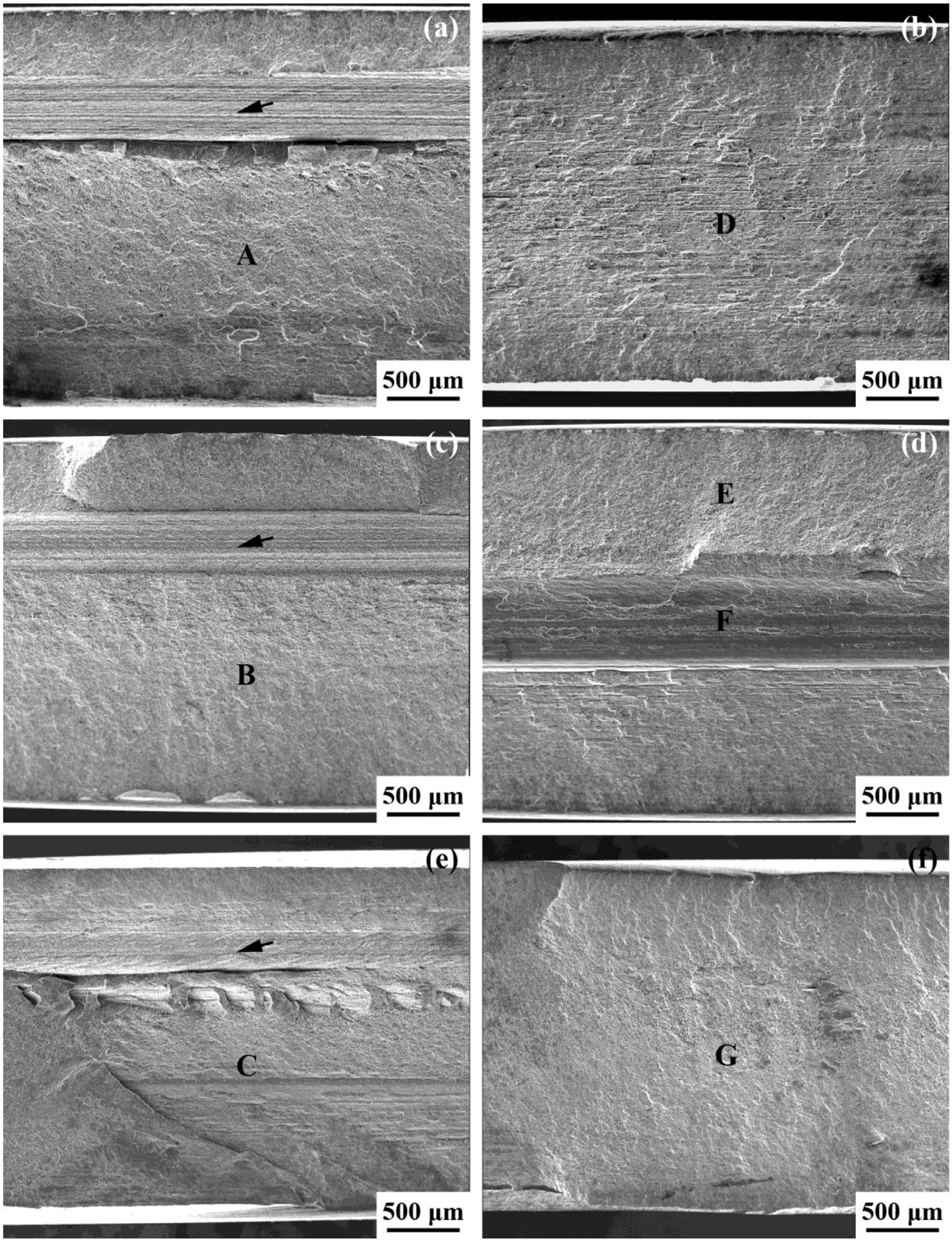

Fig. 8. Macrographic fractographs of FSW 2198-T8 joints: (a) AC-1200–200, (b) AC-1200–50, (c) AC-1200–200-AA, (d) AC-1200–50-AA, (e) WC-1200–200 and (f) WC-1200–50.

Table 3
Crystal structure and precipitation characteristics for precipitates in Al-Cu-Li-Mg-Ag-Zr alloys.

Precipitate	Crystal structure	Morphology	Orientation	Refs.
T1 (Al2CuLi) [10–10]||[−110]Al [22,53]	Hexagonal	Platelete (front view), Needle-like (side view)	(0001)||(111)Al	
θ' (Al2Cu)	Tetragonal	Platelete (front view), Needle-like (side view)	[001]||[100]Al	[22,53]
S′ (Al2CuMg)	Orthorhombic	Lath	[100]||[100]Al [010]||[02−1]Al [001]||[012]Al	[22]
δ' (Al3Li)	L12	Spherical	(111)||(111)Al	[22,53]
β' (Al3Zr)	L12	Spherical	(111)||(111)Al	[22,29]

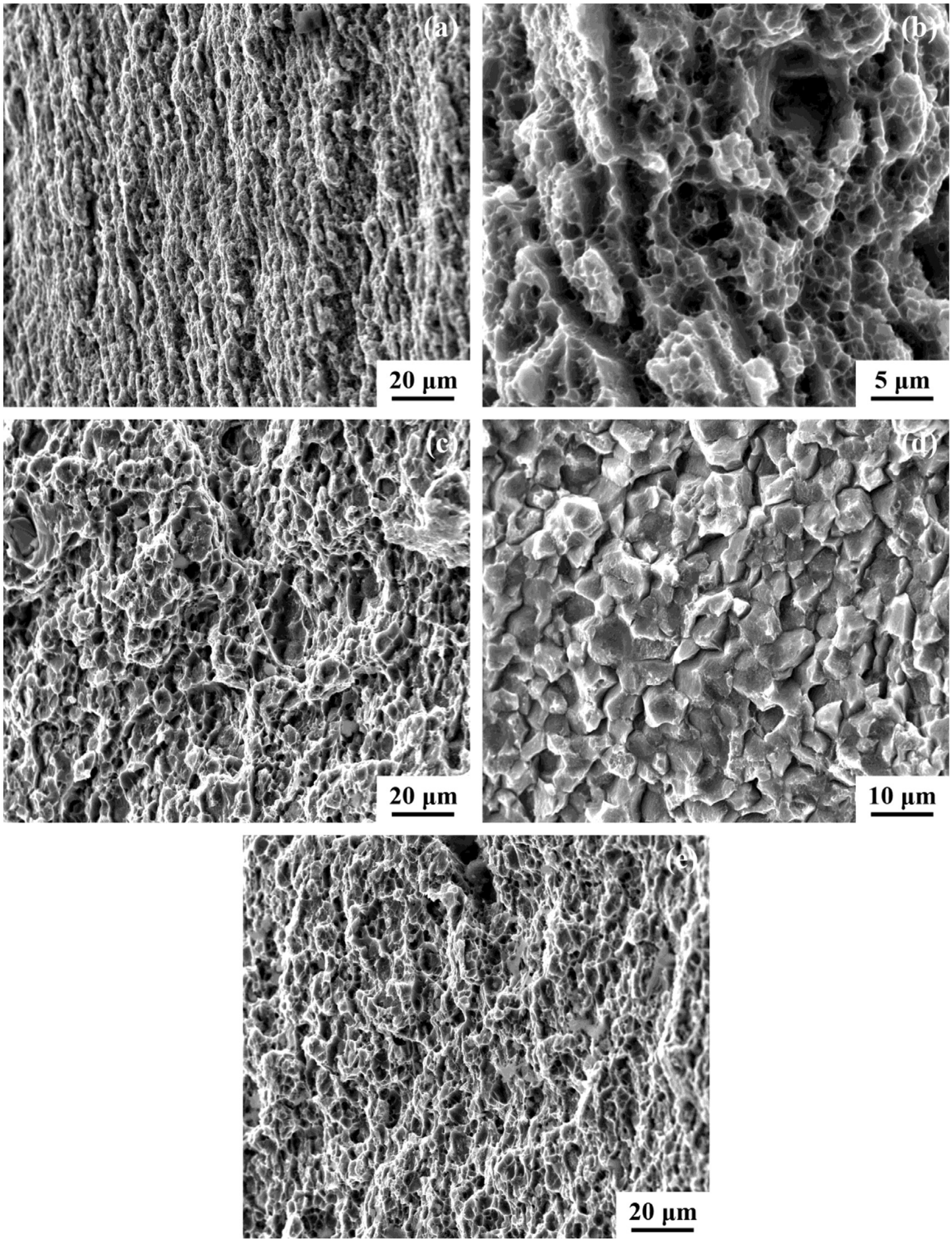

Fig. 9. Magnified fractographs of specific positions in Fig. 8: (a) and (b) magnified and further magnified images of the areas marked by arrows; (c) position A, (d) position B and (e) position C.

metrically located reflections at 1/3<220>$_{Al}$ for the <100>$_{Al}$ SAD patterns (Fig. 11(d)), as well as the two reflections at 1/3<220>$_{Al}$ and streaks along <111>$_{Al}$ direction for the <110>$_{Al}$ and <112>$_{Al}$ SAD patterns (Fig. 11(e, f)) [9,22,49,52]. θ' appears as laths lying along <200>$_{Al}$ direction in the bright field image approximately along <100>$_{Al}$ (Fig. 11(c)) [42,53] and contributes to discontinuous streaks with intensity maxima along <100>$_{Al}$ direction for the <100>$_{Al}$ SAD patterns (Fig. 11(d)) [9,54]. The presence of δ' or β' is evidenced by the characteristic superlattice reflections at 1/2<200>$_{Al}$ and 1/2<220>$_{Al}$ (Fig. 11(d–f)) [9,22,55]. It should be pointed out that δ' and β' had almost the same supperlattice reflections as well as morphologies [9,10], and they could present as Al_3(Li,Zr) particles [33]. Thus, they were not distinguished from each other and referred to as δ'/β' hereafter. It is noted that δ'/β' could hardly be found in the bright field image, which is probably related to their low volume fraction and the strong contrast induced by a high density of T_1.

Figs. 12 and 13 show TEM bright field micrographs and SAD patterns of the LHZ, respectively, of sample AC-800-200 and AC-800-200-AA. For sample AC-800-200, the LHZ experiences a sub-

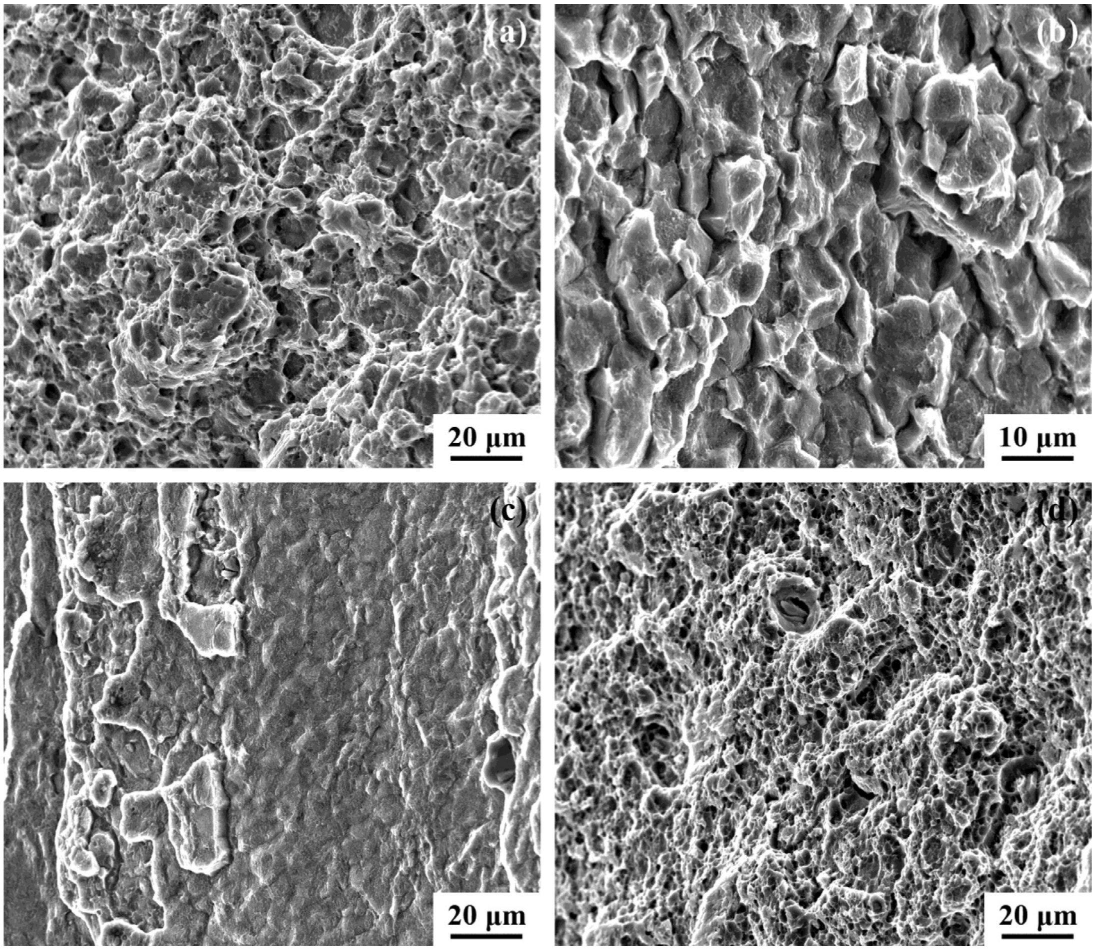

Fig. 10. Magnified fractographs of specific positions in Fig. 8: (a) position D, (b) position E, (c) position F and (d) position G.

stantial decrease in the density of T_1 and a slight decrease in the size of θ' as compared to the BM (Figs. 11(b, c) and 12(b, c)), indicating their partial dissolution. On the other hand, for sample AC-800-200-AA, post weld artificial aging leads to an increase in both the density and the size of T_1 and θ' in the LHZ when compared to sample AC-800-200 (Fig. 12(b, c, e, f)).

Figs. 14 and 15 show TEM bright field micrographs and SAD patterns of the TMAZ, respectively, of sample AC-800-200 and AC-800-200-AA. For sample AC-800-200, the TMAZ exhibits further decrease in the density of T_1 relative to that seen in the LHZ (Figs. 12(b) and 14(b)), with T_1 being sparsely populated within the grains (Fig. 14(b)). Meanwhile, no evidence of θ' is found in bright field images or SAD patterns. These results suggest that dissolution of the great majority of T_1 and complete dissolution of θ' occur in the TMAZ. In addition to T_1, small spherical precipitates with coherent strain contrast, which corresponded to δ'/β' superlattice diffraction spots, are also observed in this region (Fig. 14(b)).

For sample AC-800-200-AA, post weld artificial aging remarkably raises the density of T_1 as well as its size in the TMAZ as compared to sample AC-800-200 (Fig. 14(b, e)). Furthermore, a significant precipitation of θ' and S′ laths, lying along $<200>_{Al}$ [42,53] and $<220>_{Al}$ [22] direction, respectively, happens in the TMAZ during post weld artificial aging (Fig. 14(e, f)), as confirmed by SAD patterns. θ' contributes to streaks along $<100>_{Al}$ for the $<100>_{Al}$ and $<110>_{Al}$ SAD patterns (Fig. 15(d, e)) [9,22,54], while S′ is identified by faint streaks along $<210>_{Al}$ for the $<112>_{Al}$ SAD patterns (Fig. 15(f)) [22,49,56].

Figs. 16 and 17 show TEM bright field micrographs and SAD patterns of the NZ, respectively, of sample AC-800-200 and AC-800-200-AA. For sample AC-800-200, the NZ reveals no evidence of T_1 or θ', indicating that both of them are completely dissolved. Instead, the bright field images of the NZ is characerized by large numbers of δ'/β' (Fig. 16(b, c)), which show a higher density than those in the TMAZ (Figs. 14(b) and 16(b)). In addition to δ'/β' superlattice spots, the SAD patterns of the NZ also exhibit diffuse streaks along $<100>_{Al}$ through reflections of the matrix, suggesting the formation of GP zones (i.e., Cu monolayer) (Fig. 17(a)) [9]. The GP zones are difficult to discern in bright field images, while they could be revealed by SAD patterns.

For sample AC-800-200-AA, post weld artificial aging results in precipitation of T_1, θ' and S′ accompanied by formation of a great number of coarse precipitates with an irregular shape and orientation in the NZ (Fig. 16(e, f)). EDS analysis revealed that these incoherent precipitates were rich in Cu with the compositions of 6.7 wt.% Cu and the balance Al, whereas the surrounding matrix contained only 1.9 wt.% Cu. Thus, these precipitates are mostly likely to be equilibrium θ, which is in consistent with the results reported in previous studies [42,57]. It is worth noting that for sample AC-800-200-AA, the precipitate distributions in the NZ differ significantly from those in the TMAZ. The most apparent difference is in the much lower density of T_1 and the presence of θ in the NZ (Figs. 14(e) and 16(e)).

TEM bright field micrographs and SAD patterns of the NZ of sample WC-800-200 are shown in Fig. 18. For sample WC-800-

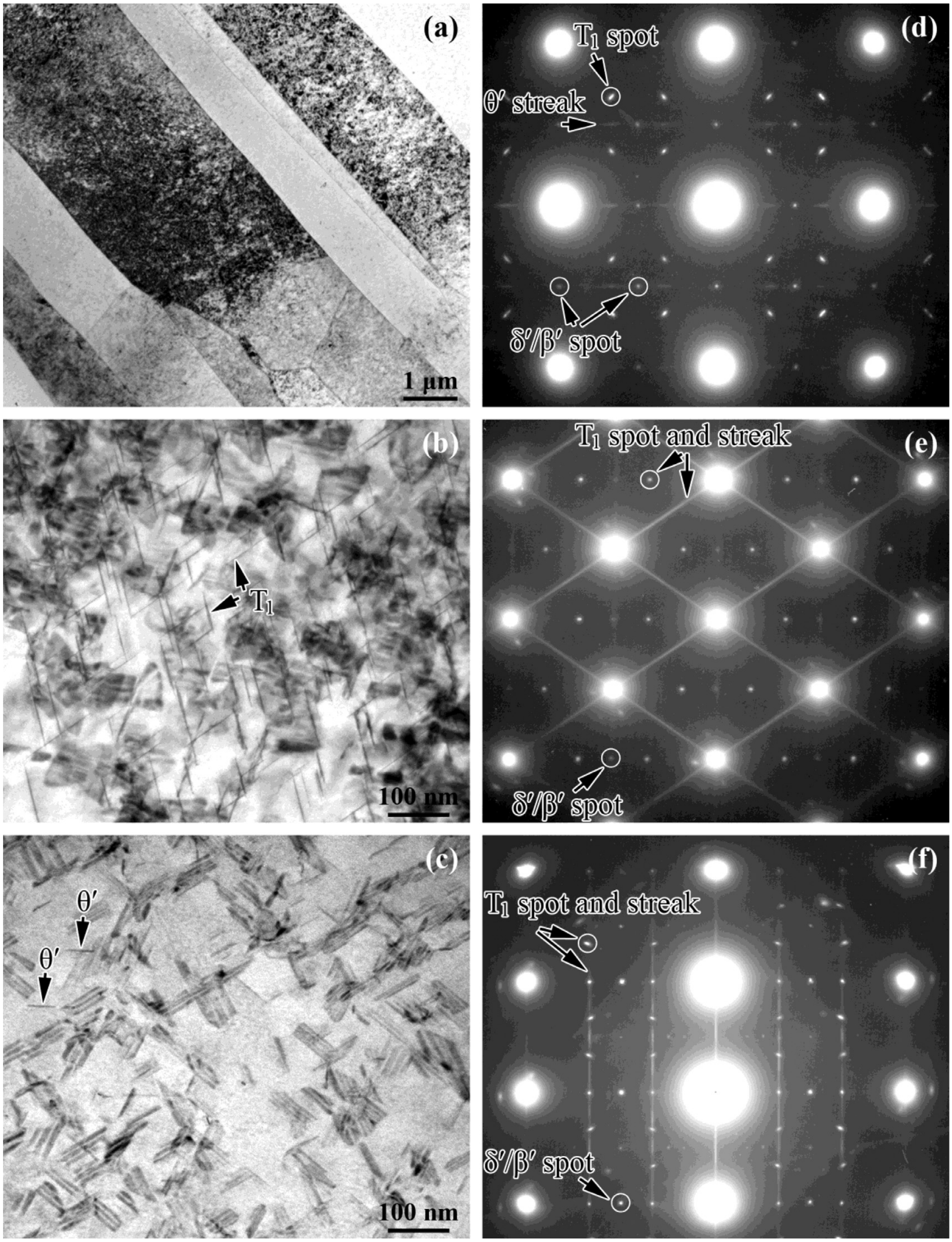

Fig. 11. TEM images of the BM: (a) low magnification bright field micrograph, (b) and (c) high magnification bright field micrographs in <110>$_{Al}$ and <100>$_{Al}$ orientations, (d), (e) and (f) SAD patterns of <100>$_{Al}$, <110>$_{Al}$ and <112>$_{Al}$ zone axes.

200, the NZ consists of δ'/β' and GP zones with T_1 and θ' being completely dissolved even under water cooling condition. However, the NZ of sample WC-800-200 displays lower density of δ'/β' but higher intensity of the streaks from GP zones as compared to sample AC-800-200 (Figs. 16(c) and 18(b); Figs. 17(a) and 18(c)). It should be pointed out that grain boundary phases along with precipitate free zones (PFZs) are formed from the HAZ to the NZ for sample AC-800-200-AA (Figs. 12(d), 14(d) and 16(d)), whereas none of them are detected in various zones of sample AC-800-200 (Figs. 12(a), 14(a) and 16(a)) or in the NZ of sample WC-800-200 (Fig. 18(a)).

4. Discussion

4.1. Effect of welding parameters on tensile properties for air cooled joints

As compared to FSW 2198-T8 joints in Refs. [30,31,33] and FSW joints of conventional precipitation-hardened Al alloys, the variations of tensile properties with welding parameters and the fracture location exhibit different features for the air cooled FSW 2198-T8 joints in the present study.

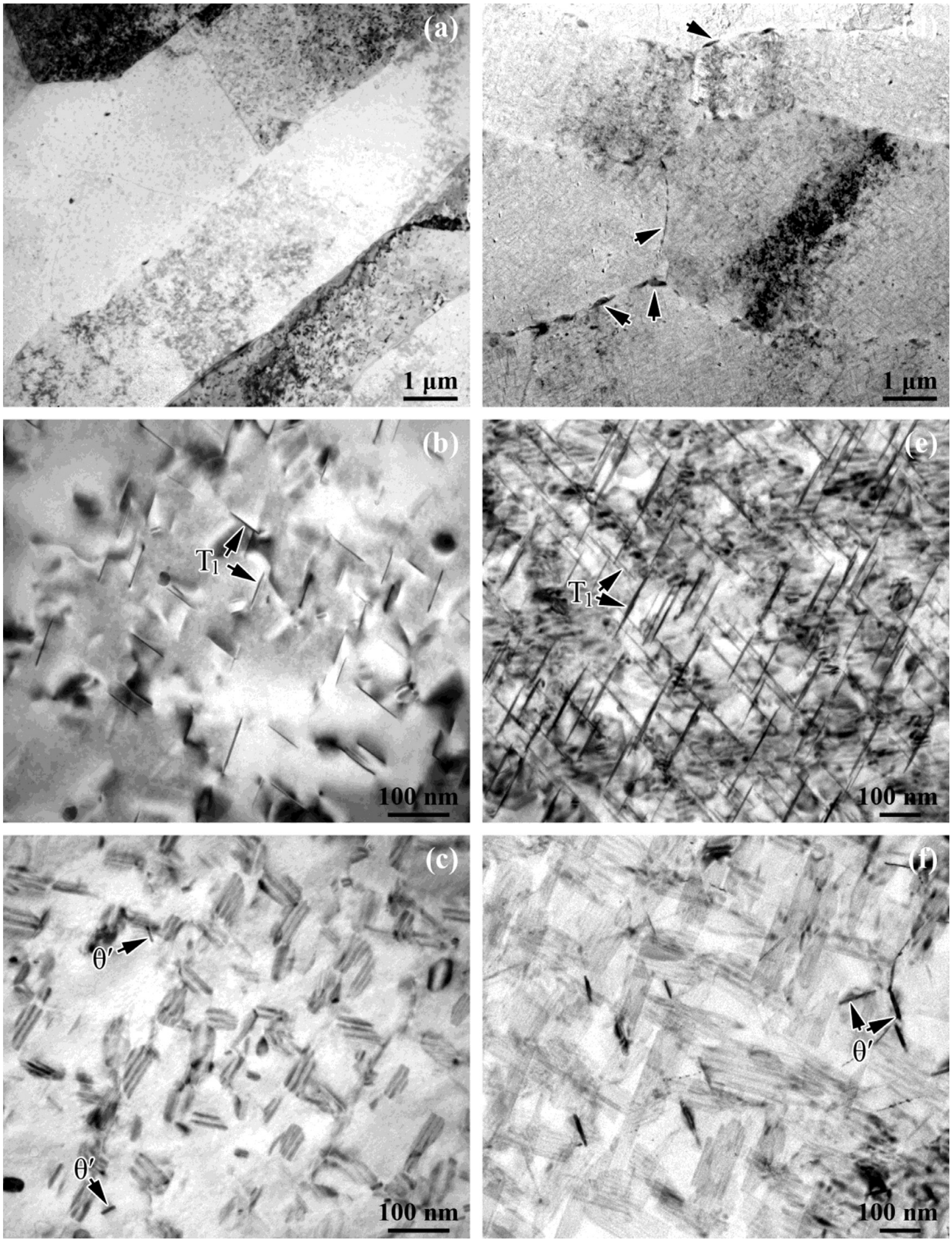

Fig. 12. TEM bright filed micrographs of the LHZ of sample (a–c) AC-800–200 and (d–f) AC-800–200-AA: (a) and (d) low magnificaiton images, (b) and (e) high magnification images in <110>$_{Al}$ orientation; (c) and (f) high magnification images in <100>$_{Al}$ orientaiton.

Firstly, for FSW 2198-T8 joints in the present study, the tensile strength of the joints hardly changes while the elongation varies for different welding parameters (Table 2). However, for FSW 2198-T8 joints in previous studies, either the joint strength and the elongation were hardly affected by the rotation rate [33], or the joint strength increased at first and then decreased with increases in the rotation rate to welding speed ratio [31]. Furthermore, the fracture occurs in the NZ rather than the LHZ (HAZ) in this study (Fig. 7(a–c)), whereas it could take place in the TMAZ or the NZ in previous studies [30,31].

The shoulder plunge depth during FSW is important for obtaining high quality joints with smooth surface. The plunge depth is connected with the pin length. A too deep plunge depth will lead to excessive flash and hence local thinning of the joints [7]. But a too shallow plunge depth will result in inefficient movement of the material from front to back of the pin, causing formation of welding defects such as surface grooves and inner channels [7]. In the present study, a plunge depth of about 0.2 mm with a 3.0 mm-length pin was adopted to guarantee enough forge force and avoid significant local thinning. The actual joint thinning can be less than

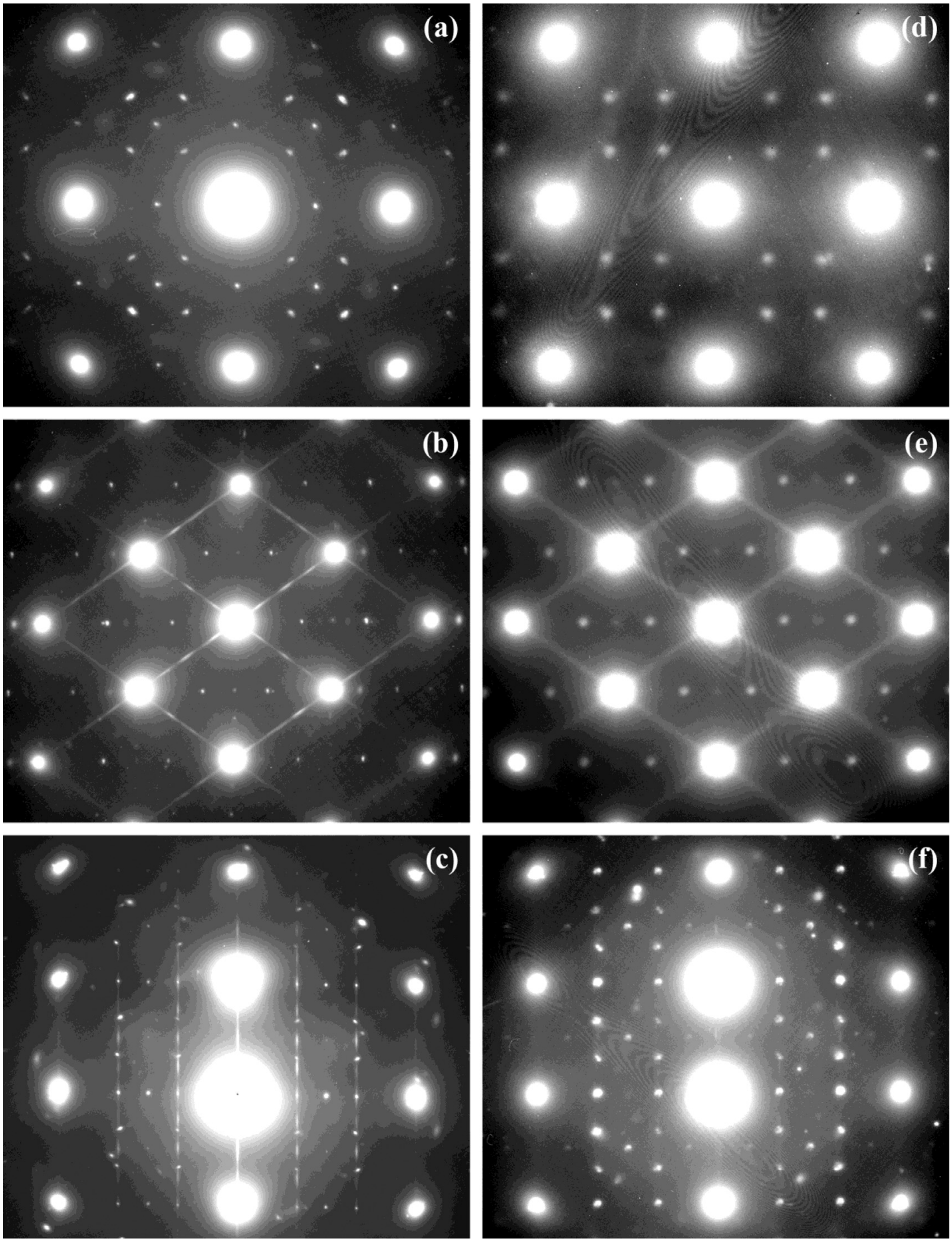

Fig. 13. TEM SAD patterns of the LHZ of sample (a–c) AC-800–200 and (d–f) AC-800–200-AA: (a) and (d) $<100>_{Al}$ zone axis, (b) and (e) $<110>_{Al}$ zone axis, (c) and (f) $<112>_{Al}$ zone axis.

0.2 mm as it is affected by heat input, material flow and concave shape of the shoulder during FSW. It is worth noting that joint thinning is inevitable so as to obtain good welding quality during FSW. When as-FSW joints were used for tensile tests, the varied cross-sectional areas across gauge part of the samples would undoubtedly influence fracture behavior and hence tensile properties of FSW 2198-T8 joints in previous studies [30,31,33]. In this respect, the data for tensile samples with joint surface plane in this study actually reflect the intrinsic tensile properties and fracture behavior of FSW 2198-T8 joints.

Secondly, the tensile strength of FSW joints of conventional precipitation-hardened Al alloys increased with increases in the welding speed but remained essentially unchanged with variations in the rotation rate, which was consistent with hardness variations of the LHZ since the joints usually fractured along the LHZ [58–61]. In this case, the LHZ played a critical role in determining tensile strength and failure locations of the joints. Nevertheless, the effect of welding parameters on joint strength and fracture location for FSW 2198-T8 joints in this study can not be attributed to hardness variations of the LHZ. This suggested that there are other factors

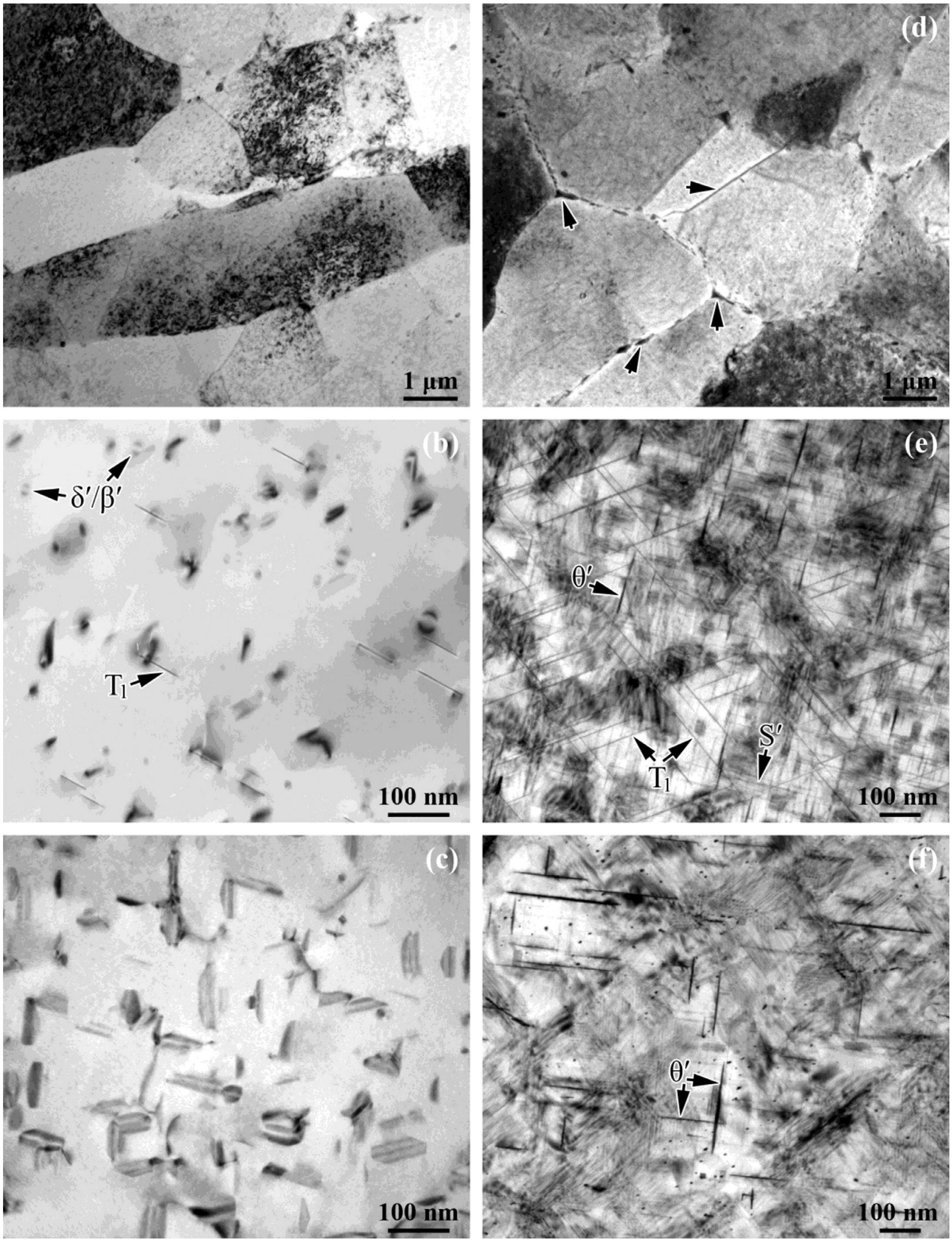

Fig. 14. TEM bright filed micrographs of the TMAZ of sample (a–c) AC-800–200 and (d–f) AC-800–200-AA: (a) and (d) low magnificaiton images, (b) and (e) high magnification images in <110>$_{Al}$ orientation, (c) and (f) high magnification images in <100>$_{Al}$ orientaiton.

accounting for the unique characteristics of the relationship between welding parameters and the intrinsic tensile properties for FSW 2198-T8 joints.

One factor that affect the intrinsic tensile properties of FSW 2198-T8 joints is connected with the unusual failure location. The LHZ hardness remarkably decreases with increases in the rotation rate or decreases in the welding speed (Fig. 6(a)), however, the intrinsic joint strength exhibits no noticeable changes with welding parameters (Table 2). This is due to that all joints fracture in the NZ rather than the LHZ (Fig. 7(a–c)) and that the NZ hardness keeps almost unchanged with variation in welding parameters (Fig. 6(a)), resulting in the comparable joint strength irrespective of welding parameters.

It should be mentioned that, for the air cooled joints, emphasis in the present study is placed on the variations of tensile properties with welding parameters as well as the precipitate evolution. The reasons for the unusual failure in the NZ rather than the LHZ for FSW 2198-T8 joints without welding defects have been reported previously by the present authors [34]. It was concluded that the combined actions of low Taylor factor and lithium segre-

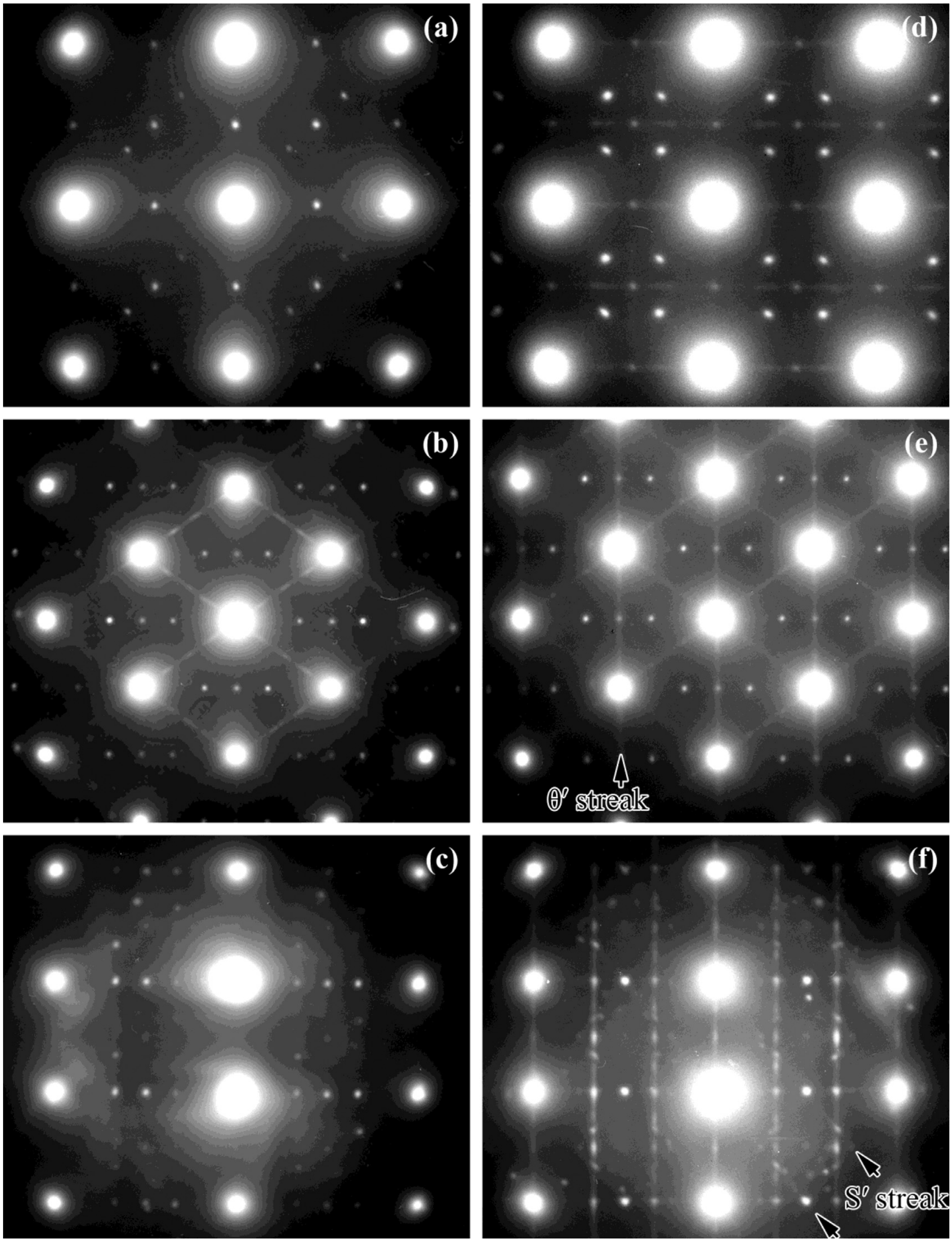

Fig. 15. TEM SAD patterns of the TMAZ of sample (a–c) AC-800–200 and (d–f) AC-800–200-AA: (a) and (d) <100>$_{Al}$ zone axis, (b) and (e) <110>$_{Al}$ zone axis, (c) and (f) <112>$_{Al}$ zone axis.

gation at the grain boundaries caused the unusual fracture in the NZ. Similar fracture phenomenon was also observed in FSW joints of other Al-Li alloys [10,62,63].

The other factor that affect the intrinsic tensile properties of FSW 2198-T8 joints is relevant to lazy S. During FSW, shear stress is generated along tangential direction of the pin surface due to rotation of the welding tool [7]. The oxide layer on the initial butt surfaces of the plates will be broken up by shear stress. The broken oxide pieces will be scattered during stirring and flow collectively along with the flow of the material in the NZ, and form the wavy lazy S [40]. It should be mentioned that clearing the oxide layer on top and butt surfaces of the plates before welding could not eliminate lazy S according to the study on FSW 7075-T651Al joints by Ren et al. [38]. They pointed out that Al alloys were apt to be oxidized and hence the oxide layer would form immediately after clearing. Moreover, the plates ahead of the welding tool would be oxidized unavoidably under thermal exposure during FSW.

The break-up and scattering degree of the oxide layer depend on the stirring extent and heat input during FSW, which is affected by the rotation rate, the welding speed, as well as the size and

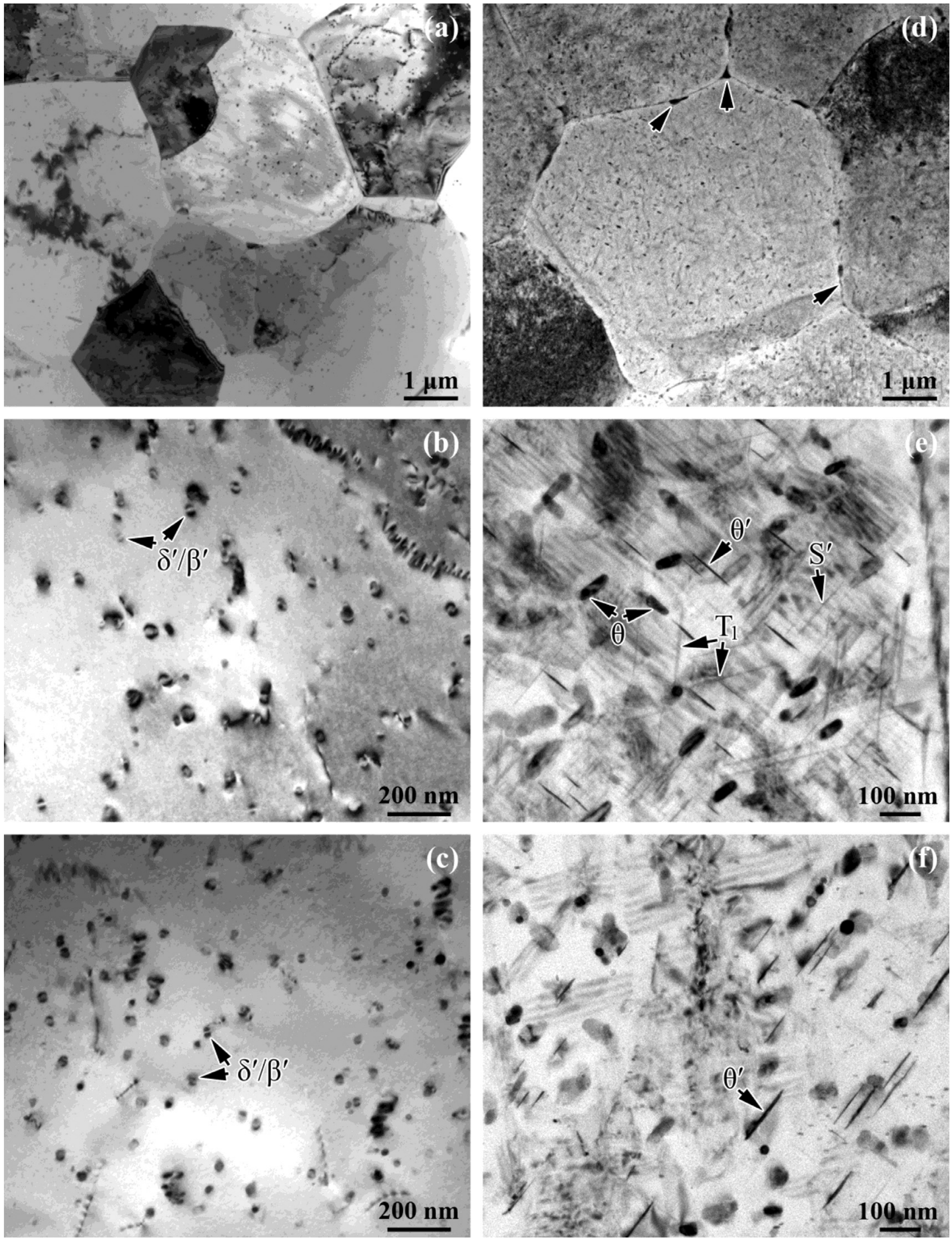

Fig. 16. TEM bright filed micrographs of the NZ of sample (a–c) AC-800–200 and (d–f) AC-800–200-AA: (a) and (d) low magnificaiton images; (b) and (e) high magnification images in <110>$_{Al}$ orientation; (c) and (f) high magnification images in <100>$_{Al}$ orientation.

configuration of the welding tool [37,39,64]. Increasing the rotation rate, decreasing the welding speed or adoption of large-sized welding tool with proper-designed shape will increase the stirring extent and heat input, and hence results in wide and dilute distribution of the oxide particles. In this case, lazy S can be eliminated. On the contrary, a decrease in the stirring extent and heat input will produce insufficient beak-up and scattering of the oxide layer. This will lead to local and dense distribution of the oxide particles and hence appearance of lazy S. Therefore, lazy S is dense and continuous in sample AC-800-200 but is faint and discontinuous in sample AC-1200-50 (Fig. 3(a, c)). In addition, unlike that in the lower part of the NZ, lazy S in the upper part of the NZ remains distinct for all the welding parameters used (Fig. 3(a–c)), which is probably related to different stirring actions induced by the rotating pin and shoulder during FSW, respectively.

Previous studies indicated that whether the joints fractured along lazy S was relevant to the hardness gap between the LHZ and the NZ, as well as dispersion extent of the oxide products [37,38,64]. Ren et al. [38] reported that post weld T6-treated FSW joints of 7075Al-T651 with homogeneous hardness distribution

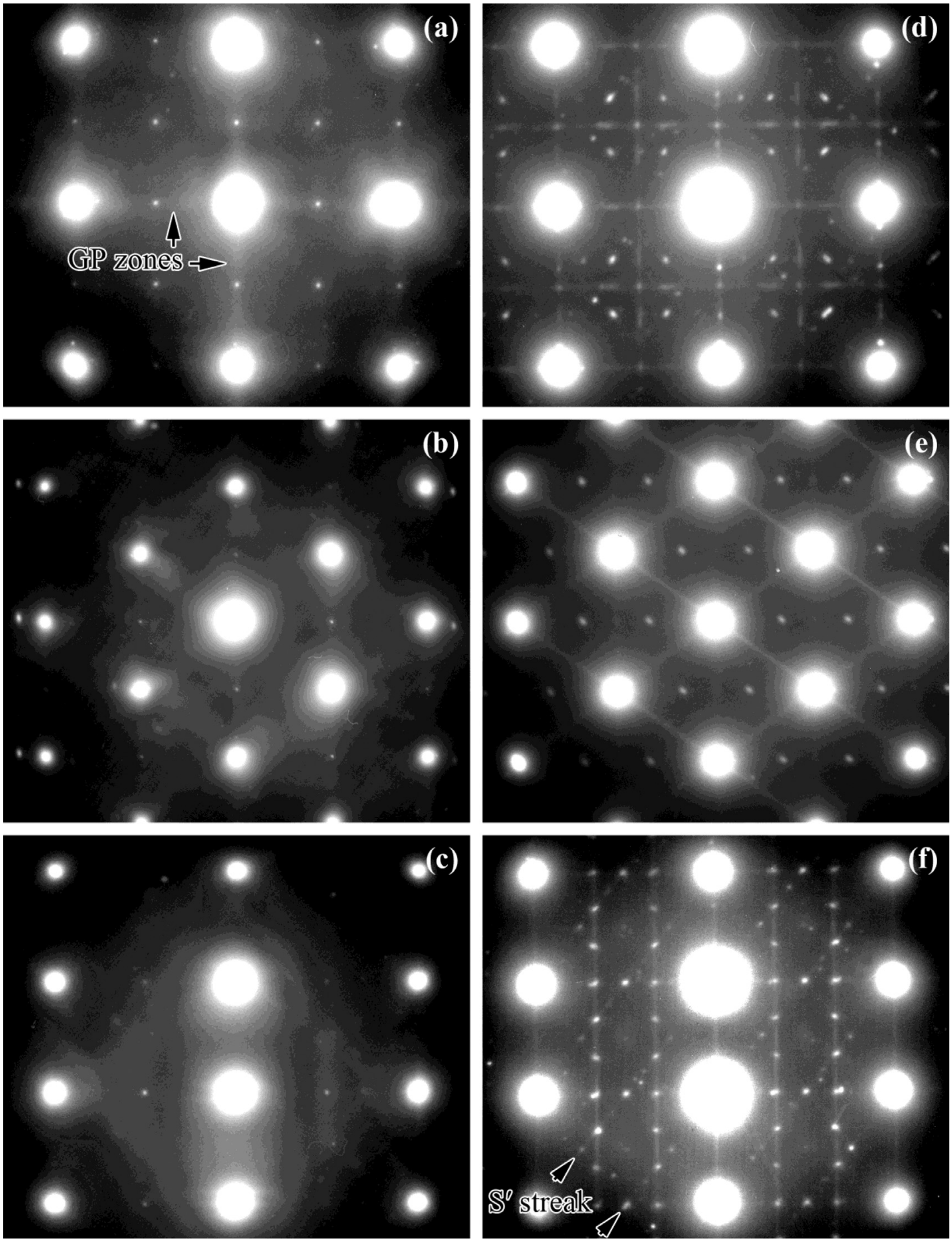

Fig. 17. TEM SAD patterns of the NZ of sample (a–c) AC-800–200 and (d–f) AC-800–200-AA: (a) and (d) <100>$_{Al}$ zone axis, (b) and (e) <110>$_{Al}$ zone axis, (c) and (f) <112>$_{Al}$ zone axis.

fractured along lazy S. Peel et al. [64] showed that for FSW 5083Al joints with low hardness plateau, lazy S was detected for all welding speeds. However, the fracture location changed from beyond the NZ to lazy S within the NZ with increasing the welding speed, due to reduced dispersion extent of the oxide products. Nevertheless, Zhang et al. [37] found that for FSW 2024Al-T351 joints with large hardness gap between the LHZ (HAZ) and the NZ, the fracture occurred along the LHZ rather than lazy S in the NZ. These studies revealed that only if both conditions, i.e., a small hardness gap between the LHZ and the NZ and a distinct lazy S with low disruption extent of the oxide products, were met, the fracture along lazy S could occur during tension.

In this study, the fracture is partially along lazy S in the upper part of the NZ for sample AC-1200-200 but is independent of lazy S for samples AC-800-200 and AC-1200-50 (Fig. 7(a–c)), which can be explained as follows. Although lazy S in the upper part of the NZ remains distinct for all samples, its tilting angle with respect to the transverse direction (i.e., loading direction during tension) is approximately 45° for sample AC-1200-200, which is larger than that for samples AC-800-200 and AC-1200-50 (Fig. 3(a–c)). This

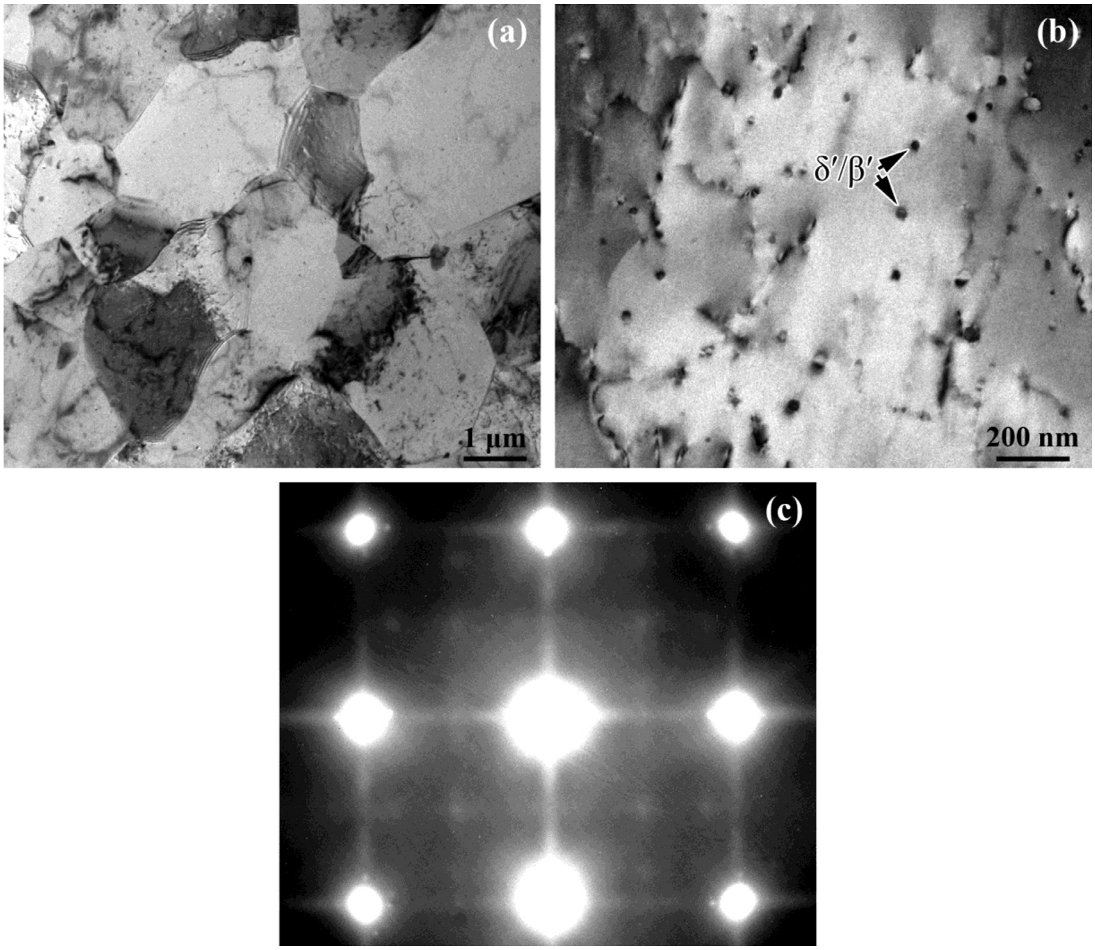

Fig. 18. TEM images of the NZ of sample WC-800–200: (a) low magnification bright field micrograph; (b) high magnification bright field micrograph in $<100>_{Al}$ orientation; (c) SAD patterns of $<100>_{Al}$ zone axis.

45° tilting angle of lazy S is consistent with the direction of maximum resolved shear stress during tension and thus is beneficial to crack propagation along lazy S. Besides, hardness gap between the LHZ and the NZ is small for sample AC-1200-200 (Fig. 6(a)). In this case, sample AC-1200-200 is more inclined to fracture along lazy S. Therefore, although lazy S is not the predominant factor accounting for the unusual failure in the NZ for FSW 2198-T8 joints [34], it plays a role in crack propagation and hence may affect tensile properties of the joints.

The comparable tensile strength for samples AC-800-200, AC-1200-200 and AC-1200-50 reveals that lazy S hardly affects the joint strength (Table 2), considering that they all fracture in the NZ with nearly identical hardness (Figs. 6(a) and 7(a–c)). In this case, it is believed that the joint strength is dominated by the hardness and hence the precipitation evolution in the NZ despite the presence of lazy S. However, fracture along lazy S leads to considerable reduction in the elongation for sample AC-1200-200 (Table 2). The fracture surface along lazy S exhibits much smaller and shallower dimples than that of the matrix (Fig. 9(a-c)), reflecting the reduced ductility. Its fracture mechanism may involve nanometer-sized dimples created at the interface between the matrix and the oxide particles [65]. The influence of lazy S on tensile properties of FSW 2198-T8 joints in this study is in agreement with the results for FSW Al-Mg-Sc joints [36] but differs from the results for FSW 5083Al joints and post weld T6-treated FSW 7075Al-T651joints [38,64], in which lazy S deteriorated the joint strength and elongation. Besides, lazy S exerted no effect on tensile properties of FSW 2024Al-T351 joints since the joints did not fail along lazy S [37]. These divergences are related to variations in density and continuity of the oxide particles along lazy S arising from different welding parameters, tools and material flow during FSW. It is noted that lazy S exerts similar effects on the fracture behavior and tensile properties for the air cooled, the water cooled and the post weld aged joints.

4.2. Effect of post weld artificial aging on microstructure and mechanical properties of the joints

4.2.1. Precipitate and hardness distribution across the joint before post weld artificial aging

The BM of 2198-T8 alloy consists of T_1, θ' and δ'/β', with T_1 being the predominant precipitate (Fig. 11). Previous studies revealed that T_1 and θ' usually precipitated during artificial aging at roughly 130–260 °C and 190 °C, respectively [14,66,67], while δ'/β' could form below 94 °C in natural aging process [68]. In addition, T_1, θ' and δ'/β' would start to dissolve at around 300 °C, 400 °C and 180 °C, respectively [26,27,66,68,69]. Typically, for FSW joints of precipitation-hardened Al alloys, the HAZ, TMAZ and NZ underwent different thermal cycles with the peak temperature varying around 250–350 °C, 350–450 °C and 475–530 °C, respectively [7,27,70,71]. Therefore, the precipitates evolves in different ways at various zones of the joints.

The high temperatures in the LHZ (HAZ) mainly cause T_1 to partially dissolve (Figs. 11(b, c) and 12

(b, c)), accounting for the observed decrease in hardness as compared to the BM (Fig. 6(a)). The higher temperatures in the

TMAZ resulte in further dissolution of T_1 and complete dissolution of θ' (Figs. 12(b, c) and 14(b, c)). The severe plastic deformation and thermal exposure in the NZ lead to complete dissolution of both T_1 and θ' (Fig. 16(b, c)).

Moreover, based on the dissolution and formation temperatures of δ'/β', for the LHZ, TMAZ and NZ, the heat of welding will make δ'/β' first dissolve and then re-precipitate from the supersaturated solution upon cooling [26,68,69]. From the LHZ towards the NZ, the increased dissolution of T_1 and θ' provides higher supersaturation extent and hence allows enhanced re-precipitation of δ'/β', along with formation of GP zones in the NZ during natural aging (Fig. 17(a)). This is responsible for the small increase in hardness (Fig. 6(a)). Thus, δ'/β' is hardly observed in the bright field images of the LHZ (Fig. 12(b)) but is distinctly visible in those of the TMAZ and NZ (Figs. 14(b) and 16(b)), although the presence of δ'/β' is evidenced by the SAD patterns in all three zones (Figs. 13(a-c), 15(a–c) and 17(a–c)).

It is noted that all precipitates are dissolved in the NZ even for sample AC-800-200 with the lowest heat input (Figs. 16(a–c) and 17(a–c)). In this case, the NZ of samples AC-1200-200 and AC-1200-50 with higher heat input will also exhibit complete dissolution of all precipitates, resulting in comparable supersaturation extent and hence similar natural aging response from δ'/β' and GP zones as compared to that of sample AC-800-200. Consequently, the NZ hardness is essentially unchanged with variation in welding parameters (Fig. 6(a)). Similar phenomenon was reported by Shukla et al. in FSW 2195-T8 Al-Li joints [10].

4.2.2. Precipitate evolution mechanism and its effect on hardness recovery during post weld artificial aging

Considering the aforementioned dissolution and precipitation temperatures of T_1, θ' and δ'/β' [14,26,27,66–69], post weld artificial aging at 180 °C for 24 h will give rise to coarsening of the pre-existing T_1 and θ', dissolution of the pre-existing δ'/β', as well as precipitation of T_1 and θ'.

For samples AC-800-200 and AC-800-200-AA, the LHZ is dominated by T_1 with small numbers of θ' (Fig. 12). In this case, the observed increase in the density and size of T_1 and θ' after post weld artificial aging is attributed to coarsening of the pre-existing T_1 and θ', accompanied by precipitation of T_1 and θ'. However, the relatively high density of the pre-existing T_1 in the LHZ (Fig. 12(b)) will reduce the solutes available for precipitation due to their coarsening rather than dissolution during post weld artificial aging. Thus, the precipitation of T_1 and θ' and the hardness recovery are limited in the LHZ (Figs. 6(b) and 12).

The TMAZ is composed of very few T_1 and some δ'/β' for sample AC-800-200 but contains a high density of T_1, θ' and S′ for sample AC-800-200-AA (Fig. 14). On the one hand, the almost complete dissolution of T_1 during welding, together with the dissolution of δ'/β' during post weld artificial aging, will bring about a remarkable increase in the solutes available for precipitation in the TMAZ as compared to the LHZ. On the other hand, the TMAZ generally exhibits high dislocation density because of highly deformed grains produced during FSW [71,72]. In the meantime, the nucleation of T_1 is known to be favored by dislocations due to reduced strain energy associated with the precipitate/matrix interface [73]. The above two aspects enable the precipitation of large numbers of T_1, θ' and S′ during post weld artificial aging and eventually result in higher hardness recovery in the TMAZ as compared to the LHZ (Figs. 6(b) and 14).

The NZ is characterized by δ'/β' and GP zones for sample AC-800-200, while it presents many coarse equilibrium θ but a low density of T_1, θ', S′ for sample AC-800-200-AA (Figs. 16 and 17(a–c)). The reasons for such precipitate evolution during post weld artificial aging are elucidated as follows. Firstly, even if the NZ is the zone where the deformation during FSW is maximal, there are few dislocations left after welding due to the highest temperature and the associated dynamic recrystallization [71,72], which will provoke a strong delay in aging kinetics of T_1 [73]. Secondly, during aging for Al-Cu alloys, the representative precipitation sequence is: supersaturated solution→GP zones→θ''→θ'→θ [74,75]. Schueller et al. [76] reported that GP zones commonly transformed into θ' when aged below the solution temperature of θ'', i.e., approximately 220 °C. Shower et al. [77] indicated that for unmodified Al-Cu alloys, θ' to θ phase transformation could occur at 200 °C, causing a rapid decrease in strength. Moreover, they pointed out that the temperature and time required for θ' to θ transformation was a function of Cu diffusivity and interfacial energy of θ', both of which were affected by microalloying [77]. In this case, for FSW 2198-T8 joints in the present study, it is believed that the pre-existing GP zones in the NZ will progressively transform into θ during post weld artificial aging at 180 °C for 24 h (Figs. 16(e) and 17(a)). The formation of many coarse θ consumed large quantities of solutes and hence lowers the precipitation potential of other strengthening precipitates. As a result, a much reduced precipitation of T_1, θ' and S′, especially T_1, and corresponding lower hardness recovery is observed in the NZ as compared to the TMAZ during post weld artificial aging (Figs. 6(b) and 16).

The above discussions indicate that aging kinetics for FSW 2198-T8 joints is strongly related to the volume fraction of both original precipitate dissolution during welding and coarse particles formed during aging, and to the dislocation density inherited from welding. Precipitate observations made in this study for FSW 2198-T8 joints are summarized in Table 4. In addition, a schematic diagram of bright field image close to $<110>_{Al}$ for precipitate evolution in FSW 2198-T8 joint is presented in Fig. 19, since the precipitates involved in this joint, such as T_1 and θ', exhibit characteristic morphologies when viewed along this orientation. In summary, the BM is composed of T_1, θ' and δ'/β' with T_1 being the main strengthening precipitates. Under air cooling condition, the LHZ is dominated by partial dissolution of T_1 and θ'. From the LHZ through the TMAZ to the NZ, further dissolution of these precipitates continues until no precipitates remain in the NZ and thus allows increased precipitation of δ'/β' and GP zones during natural aging. Post weld artificial aging leads to coarsening of relatively high density of pre-existing T_1 in the LHZ and formation of coarse equilibrium θ in the NZ, which lower the precipitation potential of strengthening precipitates and hence result in limited precipitation. In contrast, the TMAZ shows significant precipitation of T_1, θ' and S′ during aging due to almost complete dissolution of original precipitates and high dislocation density inherited from welding. Under water cooling condition, all original precipitates are completely dissolved in the NZ with precipitation of fewer δ'/β' and more GP zones streaks during cooling as compared to air cooling condition. These precipitate evolution behaviors well explain the corresponding hardness changes for FSW 2198-T8 joints.

4.2.3. Effect of post weld artificial aging on tensile properties of the joints

Indeed, post weld artificial aging enhances the hardness throughout the weld (Fig. 6(b–d)), which accounts for significant improvement in tensile strength for FSW 2198-T8 joints (Table 2). However, post weld artificial aging gives rise to formation of grain boundary precipitates and PFZs (Figs. 12(d), 14(d) and 16(d)), causing the change in fracture feature from dimpled fracture to intergranular fracture (Fig. 9(c, d)) and thus resulting in deterioration in joint ductility (Table 2).

Similar results were reported in FSW joints of peak aged 1424 Al-Li alloy [26]. However, different from varying levels of hardness recovery across FSW 2198-T8 joints in this study (Fig. 6(b–d)), post weld artificial aging led to full recovery of hardness in all zones for FSW 1424 Al-Li joints [26]. This is attributed to the nature of the

Table 4
Summary of precipitate evolution in various zones of FSW 2198-T8 joints.

Region	Sample	Precipitate evolution
BM	–	T_1, θ' and δ'/β'
LHZ	AC-800–200	T_1 and θ' partially dissolved
	AC-800–200-AA	(1) pre-existing T_1 and θ' coarsened
(2) T_1 and θ' precipitated		
TMAZ	AC-800–200	(1) T_1 further dissolved and θ' completely dissolved
(2) δ'/β' reprecipitated		
	AC-800–200-AA	(1) The pre-existing T_1 coarsened and δ'/β' dissolved
(2) T_1, θ' and S′ precipitated		
NZ	AC-800–200	(1) T_1, θ' and δ'/β' completely dissolved
(2) δ'/β' and GP zones reprecipitated		
	AC-800–200-AA	(1) pre-existing δ'/β' dissolved
(2) T_1, θ' and S′ precipitated		
(3) θ formed		
	WC-800–200	(1) T_1, θ' and δ'/β' completely dissolved
(2) δ'/β' and GP zones reprecipitated		

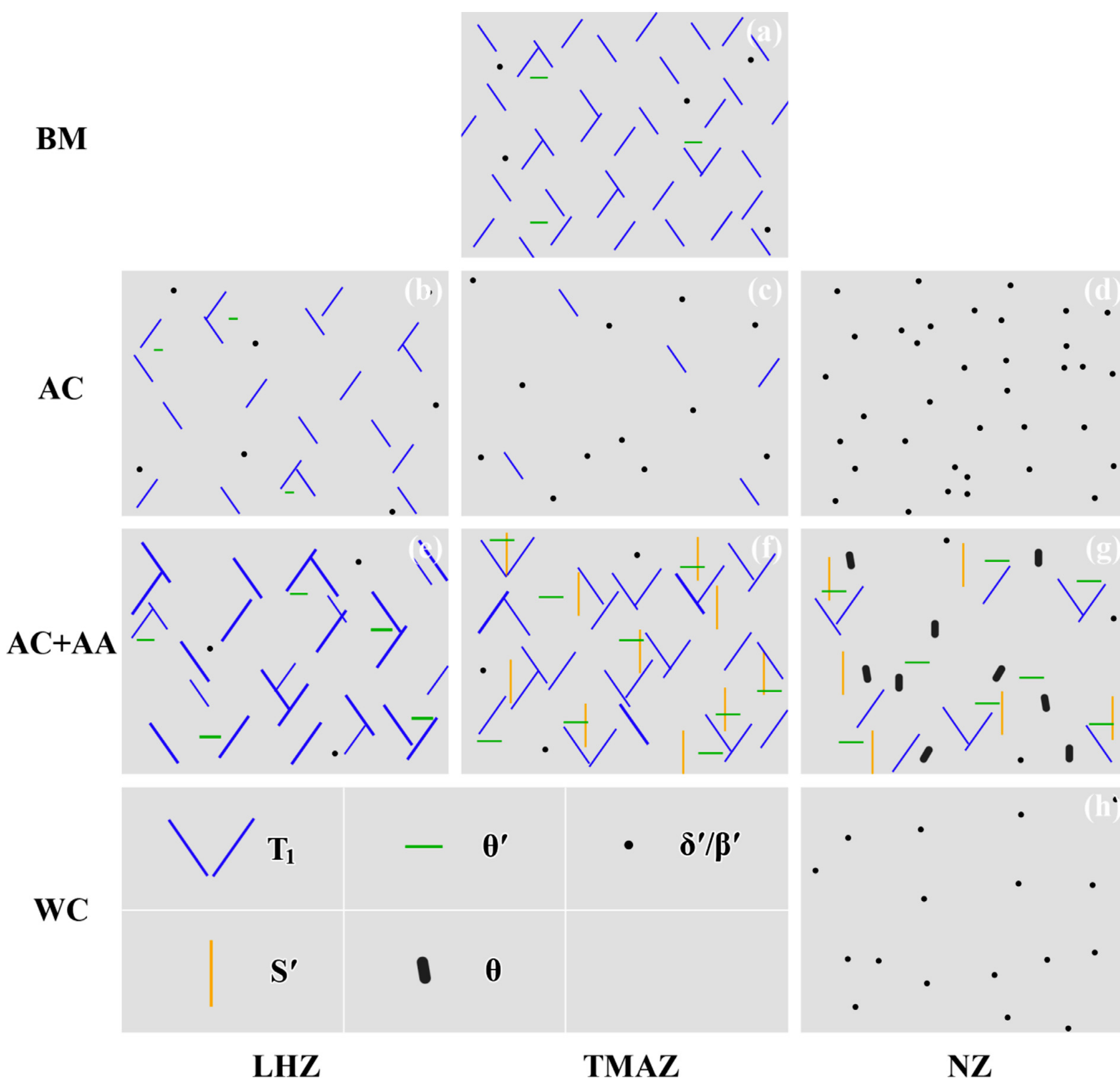

Fig. 19. Schematic diagrams of TEM bright field micrographs in $<110>_{Al}$ orientation showing precipitate evolution of FSW 2198-T8 joints.

main precipitate, i.e., δ', in 1424 Al-Li alloy [26]. δ' can completely dissolve even in the HAZ during welding because of its relatively low dissolution temperature. Also, δ' has very low interface energy, suggesting that it precipitates easily throughout the matrix. Thus, dense and homogeneous precipitation of δ' occurred from the HAZ to the NZ during post weld artificial aging, which explained the full recovery of hardness in these zones for FSW 1424 Al-Li joints [26].

Such an improvement in joint strength and a reduction in joint ductility after post weld artificial aging have been found in FSW joints of conventional peak aged precipitation-hardened Al alloys as well [12,14,18]. However, different from the case of FSW 2198-T8 joints in this study (Fig. 6(b–d)), post weld artificial aging resulted in the largest hardness recovery in the NZ for FSW joints of conventional peak aged precipitation-hardened Al alloys, although small hardness recovery was also observed in the LHZ [12,14,18,23,78]. Typically, FSW of conventional peak aged precipitation-hardened Al alloys brought about almost complete dissolution of precipitates in the NZ [14,18,23,78]. During post weld artificial aging, the NZ exhibited formation of large numbers of fine precipitates but seldom showed coarse equilibrium particles [14,18,23,78], which was in contrast to the observations for FSW 2198-T8 joints in this study (Fig. 16(e)). This difference is presumably due to the fact that the temperatures or time used for post weld artificial aging of FSW joints of conventional precipitation-hardened Al alloys are insufficient to cause extensive formation of coarse equilibrium particles in the NZ [18,23,78]. Furthermore, the aging kinetics of the main precipitates in these joints, such as θ', are believed to place weaker reliance on dislocations as compared to those of the predominant precipitate in FSW 2198-T8 joints, i.e., T_1 [25,73]. Thus, in the NZ with low dislocation density [71,72], substantial precipitation of strengthening phases could still happen during post weld artificial aging for FSW joints of conventional precipitation-hardened Al alloys [14,18,23,78].

4.3. Reason for unsuccessful improvement in tensile properties of the joints by water cooling

As compared to air cooling condition, water cooling has negligible influence on the NZ hardness (Fig. 6(b–d)). This can be explained as follows. Although water cooling leads to decreased heat input during FSW [27], the heat input in the NZ is still enough to dissolve all precipitates, allowing subsequent formation of δ'/β' and GP zones during natural aging (Fig. 18). This result is in agreement with the case of the NZ for the air cooled joint (Figs. 16(a–c) and 17(a)). Nevertheless, as compared to that of the air cooled joint, the NZ of the water cooled joint exhibits lower density of δ'/β' but higher intensity of the streaks from GP zones (Figs. 16(c) and 18(b); Figs. 17(a) and 18(c)). Kumar et al. [22] studied the effect of Li on natural aging response of Al-Cu-Li-Mg-Ag-Zr alloys. They pointed out that Li in solid solution acted as vacancy traps attributing to its high vacancy binding energy, causing a significant decrease in free vacancy available for encountering other solutes such as Cu, thereby retarding the formation of GP zones. On the other hand, these Li-vacancy pairs would serve as δ'/β' nucleation sites and facilitated the formation of δ'/β'. In addition, Zhang et al. [13] indicated that for FSW 2014Al-T6 joints, water cooling reduced the solid solution degree of solutes in the NZ as a result of lower welding peak temperatures. In this case, as compared to that of the air cooled joint in the present study, the relatively lower solid solution degree of solutes, including Li, in the NZ of the water cooled joint will bring about increased free vacancy concentration and hence account for the increase in GP zone intensity in spite of the decrease in δ'/β' density (Figs. 16(c) and 18(b); Figs. 17(a) and 18(c)).

Considering that both δ'/β' and GP zones contribute to the strength, the difference in their relative content between the NZ of the air cooled joint and that of the water cooled joint accounts for the marginal difference in the NZ hardness. Generally, the heat input and plastic deformation extent in the NZ change with variations in welding parameters, which will result in different solid solution degrees of solutes and free vacancy concentrations and hence different relative contents of δ'/β' and GP zones in the NZ [13,22]. This can explain the comparable NZ hardness for sample WC-1200-200 and the slight lower NZ hardness for samples WC-800-200 and WC-1200-50 as compared to air cooling condition. These marginal differences in the NZ hardness between the air cooled joints and the water cooled joints for different welding parameters eventually lead to corresponding differences in the joint strength (Fig. 6 and Table 2), since both the air cooled joints and the water cooled joints fracture in the NZ (Fig. 7). A recent study on FSW 2219/2195 joints by Xie et al. [79] revealed that the joint corrosion resistance was closely related to the precipitates and solid solution degree of solutes. Thus the changes in precipitate content, solid solution degree of solutes and grain size in the NZ induced by water cooling FSW can considerably alter the corrosion behavior of the joints.

The unsuccessful improvement in joint strength by water cooling for FSW 2198-T8 joints in this study differs from the result for FSW joints of peak aged 1424 Al-Li alloy [26] and typical cases for FSW joints of conventional peak aged precipitation-hardened Al alloys [15,17,20,21,80], in which water cooling managed to improve the joint strength. Unfortunately, explicit reasons for the improvement in tensile strength of FSW 1424 Al-Li joints by water cooling were not mentioned in literature [26]. For FSW joints of conventional peak aged precipitation-hardened Al alloys, the fracture location generally corresponded to the LHZ in air cooling and water cooling conditions, which commonly lied in the HAZ for the former and in the TMAZ or TMAZ/NZ boundary for the latter [15,17,21,80]. Moreover, water cooling enhanced the LHZ hardness due to lower precipitate coarsening level and narrower PFZs [15,17,20,21,80], and consequently resulted in higher joint strength as compared to air cooling condition [15,17,20,21,80].

5. Conclusions

(1) FSW 2198-T8 joints were successfully produced at 800 rpm–200 mm/min, 1200 rpm–200 mm/min and 1200 rpm–50 mm/min in both air cooling and water cooling conditions, and no welding defects other than lazy S were observed in the NZ.
(2) Under air cooling condition, the LHZ was located in the HAZ. The BM consisted of T_1, θ' and δ'/β'. T_1 and θ' partially dissolved in the LHZ, causing the sharp decrease in hardness. From the LHZ through the TMAZ to the NZ, these precipitates further dissolved until no precipitates remained in the NZ, which allowed greater natural aging response from δ'/β' and GP zones and thus accounted for the slight increase in hardness.
(3) After post weld artificial aging, hardness recovered across the joint with varying levels of improvement. In the TMAZ, the almost complete dissolution of original precipitates during welding provided substantial solutes available for precipitation, and the high dislocation density inherited from welding favored the nucleation of T_1. These two factors enabled significant precipitation of T_1, θ' and S' during aging and hence resulted in largest recovery in hardness. However, during aging, the coarsening of relatively high density of pre-existing T_1 in the LHZ and the formation of coarse θ in the NZ lowered the precipitation potential of other strengthening precipitates, leading to smaller recovery in hardness.

(4) As compared to air cooling condition, the LHZ was shifted into the TMAZ by water cooling, while marginal differences in the NZ hardness under both conditions were observed since all precipitates completely dissolved in the NZ even under water cooling condition.
(5) For the air cooled joints, the intrinsic tensile strength hardly changed with a joint efficiency reaching 81.3% whereas the elongation varied for different welding parameters, which was linked to failure in the NZ with nearly identical hardness rather than the LHZ with large hardness gap, and fracture along lazy S. After post weld artificial aging, the joint strength was effectively enhanced with a maximum joint efficiency of 87.3% achieved. As compared to air cooling condition, the joint strength was not improved by water cooling, since the fracture under both conditions occurred in the NZ with comparable hardness.

Acknowledgments

This work was supported by the Excellent Youth Foundation of Liaoning Province (No. 2021-YQ-01), Natural Science Foundation of Liaoning Province (No. 2021-MS-011) and National Natural Science Foundation of China (No. U1760201).

References

[1] T. Dursun, C. Soutis, Mater. Des. 56 (2014) 862–871.
[2] Y. Wang, S. Zhang, R. Wu, N. Turakhodjaev, L. Hou, J. Zhang, S. Betsofen, J. Mater. Sci. Technol. 61 (2021) 197–203.
[3] M.X. Milagre, U. Donatus, N.V. Mogili, R.M.P. Silva, B.V.G. de Viveiros, V.F. Pereira, R.A. Antunes, C.S.C. Machado, J.V.S. Araujo, I. Costa, J. Mater. Sci. Technol. 45 (2020) 162–175.
[4] A. Steuwer, M. Dumont, J. Altenkirch, S. Birosca, A. Deschamps, P.B. Prangnell, P.J. Withers, Acta Mater. 59 (2011) 3002–3011.
[5] S.D. Ji, Q. Wen, Z.W. Li, J. Mater. Sci. Technol. 48 (2020) 23–30.
[6] S.M.A.K. Mohammed, Y.D. Jaya, A. Albedah, X.Q. Jiang, D.Y. Li, D.L. Chen, Int. J. Fatigue 141 (2020) 105869.
[7] R.S. Mishra, Z.Y. Ma, Mater. Sci. Eng. R 50 (2005) 1–78.
[8] S.D. Ji, Y.Y. Jin, Y.M. Yue, S.S. Gao, Y.X. Huang, L. Wang, J. Mater. Sci. Technol. 29 (2013) 955–960.
[9] R.W. Fonda, J.F. Bingert, Metall. Mater. Trans. A 37 (2006) 3593–3604.
[10] A.K. Shukla, W.A. Baeslack, Sci. Technol. Weld. Join. 14 (2009) 376–387.
[11] F.C. Liu, Y. Hovanski, M.P. Miles, C.D. Sorensen, T.W. Nelson, J. Mater. Sci. Technol. 34 (2018) 39–57.
[12] E.A. El-Danaf, M.M. El-Rayes, Mater. Des. 46 (2013) 561–572.
[13] Z. Zhang, B.L. Xiao, Z.Y. Ma, Mater. Sci. Eng. A 614 (2014) 6–15.
[14] Z. Zhang, B.L. Xiao, Z.Y. Ma, Mater. Charact. 106 (2015) 255–265.
[15] R.D. Fu, Z.Q. Sun, R.C. Sun, Y. Li, H.J. Liu, L. Liu, Mater. Des. 32 (2011) 4825–4831.
[16] M.B. Lezaack, A. Simar, Mater. Sci. Eng. A 807 (2021) 140901.
[17] H. Lin, Y. Wu, S. Liu, X. Zhou, Mater. Charact. 141 (2018) 74–85.
[18] H.J. Liu, Y.C. Chen, J.C. Feng, Mater. Sci. Technol. 22 (2006) 237–241 -lond.
[19] C. Sharma, D.K. Dwivedi, P. Kumar, Mater. Des. 43 (2013) 134–143.
[20] S. Sinhmar, D.K. Dwivedi, Mater. Sci. Eng. A 684 (2017) 413–422.
[21] M.A. Wahid, A.N. Siddiquee, Z.A. Khan, N. Sharma, Mater. Res. Express 5 (2018) 046512.
[22] K.S. Kumar, S.A. Brown, J.R. Pickens, Acta Mater. 44 (1996) 1899–1915.
[23] S. Malopheyev, I. Vysotskiy, V. Kulitskiy, S. Mironov, R. Kaibyshev, Mater. Sci. Eng. A 662 (2016) 136–143.
[24] Y. Lin, C. Lu, C. Wei, Z. Zheng, Adv. Eng. Mater. 20 (2018) 1700652.
[25] B. Malard, F. De Geuser, A. Deschamps, Acta Mater. 101 (2015) 90–100.
[26] H. Sidhar, N.Y. Martinez, R.S. Mishra, J. Silvanus, Mater. Des. 106 (2016) 146–152.
[27] H. Sidhar, R.S. Mishra, Mater. Des. 110 (2016) 60–71.
[28] J. Zhang, X.S. Feng, J.S. Gao, H. Huang, Z.Q. Ma, L.J. Guo, J. Mater. Sci. Technol. 34 (2018) 219–227.
[29] C. Gao, Z. Zhu, J. Han, H. Li, Mater. Sci. Eng. A 639 (2015) 489–499.
[30] T. Le Jolu, T.F. Morgeneyer, A.F. Gourgues-Lorenzon, Sci. Technol. Weld. Join. 15 (2010) 694–698.
[31] W. Li, R. Jiang, Z. Zhang, Y.E. Ma, Adv. Eng. Mater. 15 (2013) 1051–1058.
[32] N. Nayan, M. Yadava, R. Sarkar, S.V.S.N. Murty, N.P. Gurao, S. Mahesh, M.J.N.V. Prasad, I. Samajdar, Mater. Charact. 159 (2020) 110002.
[33] J. Rao, E.J. Payton, C. Somsen, K. Neuking, G. Eggeler, A. Kostka, J.F. dos Santos, Adv. Eng. Mater. 12 (2010) 298–303.
[34] Y. Tao, D.R. Ni, B.L. Xiao, Z.Y. Ma, W. Wu, R.X. Zhang, Y.S. Zeng, Mater. Sci. Eng. A 693 (2017) 1–13.
[35] H.B. Chen, K. Yan, T. Lin, S.B. Chen, C.Y. Jiang, Y. Zhao, Mater. Sci. Eng. A 433 (2006) 64–69.
[36] Y. Tao, Z. Zhang, D.R. Ni, D. Wang, B.L. Xiao, Z.Y. Ma, Mater. Sci. Eng. A 612 (2014) 236–245.
[37] Z. Zhang, B.L. Xiao, Z.Y. Ma, Metall. Mater. Trans. A 44 (2013) 4081–4097.
[38] S.R. Ren, Z.Y. Ma, L.Q. Chen, Mater. Sci. Eng. A 479 (2008) 293–299.
[39] Y.S. Sato, H. Takauchi, S.H.C. Park, H. Kokawa, Mater. Sci. Eng. A 405 (2005) 333–338.
[40] Y.S. Sato, F. Yamashita, Y. Sugiura, S.H.C. Park, H. Kokawa, Scr. Mater. 50 (2004) 365–369.
[41] V. Richter-Trummer, E. Suzano, M. Beltrao, A. Roos, J.F. dos Santos, P.M.S.T. de Castro, Mater. Sci. Eng. A 538 (2012) 81–88.
[42] R.W. Fonda, J.F. Bingert, Metall. Mater. Trans. A 35 (2004) 1487–1499.
[43] B. Heinz, B. Skrotzki, Metall. Mater. Trans. B 33 (2002) 489–498.
[44] K.V. Jata, K.K. Sankaran, J.J. Ruschau, Metall. Mater. Trans. A 31 (2000) 2181–2192.
[45] P.M.G.P. Moreira, T. Santos, S.M.O. Tavares, V. Richter-Trummer, P. Vilaca, P.M.S.T. de Castro, Mater. Des. 30 (2009) 180–187.
[46] W. Xu, J. Liu, G. Luan, C. Dong, Mater. Des. 30 (2009) 3460–3467.
[47] A.A. Zadpoor, J. Sinke, R. Benedictus, R. Pieters, Mater. Sci. Eng. A 494 (2008) 281–290.
[48] P.L. Niu, W.Y. Li, D.L. Chen, J. Mater. Sci. Technol. 73 (2021) 91–100.
[49] A.K. Shukla, W.A. Baeslack, Scr. Mater. 56 (2007) 513–516.
[50] Y. Tao, Z. Zhang, B.H. Yu, P. Xue, D.R. Ni, B.L. Xiao, Z.Y. Ma, Mater. Charact. 168 (2020) 110524.
[51] N. Boukos, E. Flouda, C. Papastaikoudis, J. Mater. Sci. 33 (1998) 3213–3218.
[52] Y. Ma, X. Zhou, G.E. Thompson, T. Hashimoto, P. Thomson, M. Fowles, Mater. Chem. Phys. 126 (2011) 46–53.
[53] H. Li, Y. Tang, Z. Zeng, Z. Zheng, F. Zheng, Mater. Sci. Eng. A 498 (2008) 314–320.
[54] A.K. Mukhopadhyay, Metall. Mater. Trans. A 33 (2002) 3635–3648.
[55] Y. Wang, X. Ma, G. Zhao, X. Xu, X. Chen, C. Zhang, J. Mater. Sci. Technol. 82 (2021) 161–178.
[56] M.J. Starink, N. Gao, N. Kamp, S.C. Wang, P.D. Pitcher, I. Sinclair, Mater. Sci. Eng. A 418 (2006) 241–249.
[57] J.G. Jung, J.S. Park, Y.K. Lee, Met. Mater. Int. 19 (2013) 147–152.
[58] F.C. Liu, Z.Y. Ma, Metall. Mater. Trans. A 39 (2008) 2378–2388.
[59] Z.Y. Ma, A.H. Feng, D.L. Chen, J. Shen, Crit. Rev. Solid State 43 (2018) 269–333.
[60] S.R. Ren, Z.Y. Ma, L.Q. Chen, Scr. Mater. 56 (2007) 69–72.
[61] Z. Zhang, B.L. Xiao, Z.Y. Ma, J. Mater. Sci. 47 (2012) 4075–4086.
[62] O. Hatamleh, Int. J. Fatigue 31 (2009) 974–988.
[63] H. Liu, Y. Hu, C. Dou, D.P. Sekulic, Mater. Charact. 123 (2017) 9–19.
[64] M. Peel, A. Steuwer, M. Preuss, P.J. Withers, Acta Mater. 51 (2003) 4791–4801.
[65] T.L. Jolu, T.F. Morgeneyer, A. Denquin, M. Sennour, A. Laurent, J. Besson, A.F. Gourgues-Lorenzon, Metall. Mater. Trans. A 45 (2014) 5531–5544.
[66] H. Qin, H. Zhang, H. Wu, Mater. Sci. Eng. A 626 (2015) 322–329.
[67] J.A. Schneider, A.C. Nunes, P.S. Chen, G. Steele, J. Mater. Sci. 40 (2005) 4341–4345.
[68] J. Goebel, M. Reimann, A. Norman, J.F. dos Santos, J. Mater. Process. Technol. 245 (2017) 37–45.
[69] A. Deschamps, M. Garcia, J. Chevy, B. Davo, F. De Geuser, Acta Mater. 122 (2017) 32–46.
[70] O. Frigaard, O. Grong, O.T. Midling, Metall. Mater. Trans. A 32 (2001) 1189–1200.
[71] M.W. Mahoney, C.G. Rhodes, J.G. Flintoff, R.A. Spurling, W.H. Bingel, Metall. Mater. Trans. A 29 (1998) 1955–1964.
[72] C. Genevois, A. Deschamps, A. Denquin, B. Doisneau-cottignies, Acta Mater. 53 (2005) 2447–2458.
[73] W.A. Cassada, G.J. Shiflet, E.A. Starke, Metall. Mater. Trans. A 22 (1991) 299–306.
[74] A. Biswas, D.J. Siegel, C. Wolverton, D.N. Seidman, Acta Mater. 59 (2011) 6187–6204.
[75] S.Y. Hu, M.I. Baskes, M. Stan, L.Q. Chen, Acta Mater. 54 (2006) 4699–4707.
[76] R.D. Schueller, F.E. Wawner, A.K. Sachdev, J. Mater. Sci. 29 (1994) 424–435.
[77] P. Shower, J.R. Morris, D. Shin, B. Radhakrishnan, L.F. Allard, A. Shyam, Materialia 5 (2019) 100185.
[78] A. Simar, Y. Brechet, B. de Meester, A. Denquin, T. Pardoen, Mater. Sci. Eng. A 486 (2008) 85–95.
[79] Y. Xie, X. Meng, F. Wang, Y. Jiang, X. Ma, L. Wan, Y. Huang, Corros. Sci. 192 (2021) 109800.
[80] H.J. Zhang, H.J. Liu, L. Yu, J. Mater. Eng. Perform. 21 (2012) 1182–1187.